mgr inż. Bartosz Kraszewski

CAPTURING RAPID NONLINEAR PHENOMENA USING COUPLED THERMAL FLUID-SOLID INTERACTION NUMERICAL ANALYSIS

Doctoral thesis submitted to
the Scientific Council
of the Institute of Fluid-Flow Machinery
of the Polish Academy of Sciences

Thesis supervisor:
prof. dr hab. inż. Janusz Badur

Gdańsk, June 2024

I would like to express my gratitude to
prof. dr hab. inż. Janusz Badur, for the idea for
this dissertation and the scientific inspiration.

I would like to thank dr inż. Janusz Telega
for his invaluable help with the construction of
the measurement stand.

Finally, I would like to express my sincere
thanks to my parents and my wife for their
continuous support.

Computations were carried out using the computers of Center of Informatics Tricity Academic Supercomputer & Network.

Abstract

The concept of Fluid - Solid Interaction has already appeared in the literature in the 1970s. Taking additionally into account the current state of advancement of Computational Solid Dynamics as well as Computational Fluid Dynamics methods, the Thermal Fluid-Solid Interaction (Thermal FSI) methodology seems remarkably undeveloped. Given the contemporary industrial challenges in the fields of power engineering, aviation and rocket transportation, as well as the current state of knowledge of Thermal FSI methodology in the literature, two objectives have been identified for this dissertation. The first is to determine whether contemporary commercial numerical tools are suitable for simulating fast, non-linear thermal phenomena with Thermal FSI methodology for industrial purposes. The second is to compare and demonstrate the advantages and disadvantages of the Thermal-FSI method in comparison with the Thermal Structural and Conjugated Heat Transfer methods. In addition, a condition was also imposed to reproduce the non-linear behaviour of the structures.

For this purpose, an open thin-walled container was selected for testing after an initial selection. The container was characterised by repeatable buckling of the bottom on contact with hot water. A test rig was then prepared for the selected object, in which hot water was dispensed into the bottom of the tank in a controlled manner. Here, the displacement of the tank bottom, its temperature as well as the inlet water temperature were measured at selected points.

The experiment was then reproduced numerically, using the two-way Thermal FSI method with the ANSYS Workbench package. The fluid domain, using the Volume of Fluid method in Fluent was coupled using the System Coupling module to the solid domain in the Mechanical module. Uncoupled Conjugated Heat Transfer and Thermal Structural analyses were also carried out for comparison. Finally, the results from the three analyses were collated, determining their deviations from experiment. The Thermal FSI methodology not only provided the smallest deviation, but was also the only one able to capture the non-linear buckling behaviour of the structure.

Contents

Symbols and abbreviations

Abbrevations

CFD	Computational Fluid Dynamics
CHT	Conjugated Heat Transfer
CSD	Computational Solid Dynamics
EU	European Union
FEA	Finite Element Analysis
FEM	Finite Element Method
FSI	Fluid-Structure Interaction/Fluid-Solid Interaction
FVM	Finite Element Method
HDPE	High Density Polyethylene
HMH	Huber-Mises-Hencky
VOF	Volume of Fluid

Indexes

0	principal (stress), reference (temperature)
a	air
c	convective
d	diffusive (flux), deviator (stress)
e	elastic
F	fluid
k	fluid turbulence kinetic energy
L	linear
NL	nonlinear
ω	fluid turbulence specific dissipation rate
s	surface
S	Solid
T	total
th	thermal
v	volumetric
w	water
x, y, z	directional component reference

Variables

B	fluid buoyancy term
$\mathbf{B}$	strain-displacement matrix
$\mathbf{C}$	damping matrix
C_p	specific heat
D	fluid turbulence cross-diffusion term
$\mathbf{D}$	elasticity matrix
e	total energy
$\mathbf{f}$	external force vector
$\mathcal{F}$	surface flux
G	fluid turbulence production term
$\mathbf{I}$	unit tensor
k	fluid turbulence kinetic energy
$\mathbf{K}$	stiffness matrix
$\dot{m}$	mass flow
$\mathbf{M}$	mass matrix
$\mathbf{n}$	normal vector
p	pressure
$\mathbf{q}$	heat flux vector
$\mathbf{Q}$	load matrix
$\mathcal{S}$	source flux
t	time
T	temperature
$\mathbf{T}$	tensor of viscous stresses
u	internal energy
$\mathbf{u}$	displacement vector
$\mathcal{U}$	theoretical scalar quantity
$\mathbf{v}$	velocity vector
V	volume
$\mathbf{V}$	velocity matrix
$\dot{V}$	volume flow
Y	fluid turbulent dissipation term

α	phase fraction, coefficient of linear expansion
β	coeff. of thermal conductivity
$\mathit{\Gamma}$	effective diffusivity
$\boldsymbol{\varepsilon}$	elastic strain tensor
κ	curvature of a phase boundary
μ	viscosity
ρ	density
σ	component of stress tensor, surface tension coeff.
$\boldsymbol{\sigma}$	stress tensor

τ	component of viscous shear stress tensor
$\boldsymbol{\tau}$	viscous shear stress tensor
ω	fluid turbulence specific dissipation rate

Chapter 1

Introduction

1.1 Motivation

For a long time now, global trends in mechanical engineering have been changing significantly. There has been a definite shift away from the construction casualness, or even a certain prodigality, of the Industrial Revolution era. The current direction is given by the aspects of efficiency, ecology and material economy. The imposed requirements are met by designing new structures with increasingly precise tools, using common as well as new materials.

One sector for which meeting today's demands is a real challenge is the thermal power industry. The approval of the Kyoto Protocol in 1997 [1] began the fight against greenhouse gas emissions, setting a series of tasks in the power engineering field. This has contributed to the modification of combustion and filtration methods in thermal power plants, as well as providing additional motivation to increase the efficiency not only of new units, but also of old ones through retrofits. However, greater challenges were brought about by a 2009 European Union directive [2] requiring a significant increase in the share of renewable energy sources in energy systems. As photovoltaic panels and wind farms generate electricity in a mostly unpredictable manner, stabilization of the power grid becomes severely difficult. This forces the steam turbines to change loads more frequently and to start up and shut down more often. These processes are demanding because, due to thermal expansion and stresses, they require close monitoring and take hours to complete [3]. Here, not only phenomena such as rotor extension and turbine hull bending have to be predicted [4], but also the behaviour of auxiliary equipment such as valves [5]. In the end, what emerges here is the necessity to manage computational methods for unsteady, relatively sudden thermal loads in order to meet present-day requirements.

Another industry that has had to adapt rather abruptly to modern economic as well as environmental requirements is aviation. Between 2005 and 2017 alone, an average reduction in fuel consumption per passenger of 24% was achieved [6]. This was influenced, among other things, by the Emissions Trading System, which has been in force in the EU since 2012. However, with the EU's adoption of the "Fit for 55" package, further reductions in aviation emissions will be required. The new directives additionally assume the use of advanced biofuels as well as hydrogen [7]. This means that aviation engineering will not only continue to focus on reducing the weight of aircraft, through the use of new structures and materials, but also on engines operating under completely new combustion conditions. Using the example of documented failures of components such as the spray bars of a jet engine afterburner [8] or jet fuel starter [9], it can be seen that thermal fatigue is one of the current technological problems. Given the new requirements, it seems that these problems will intensify. Thus, the need for a more precise prediction of the behaviour of the structure under varying thermal loads can again be detailed here - especially in an industry where there is no room for design errors.

It is worth mentioning one more sector that has gained rapid momentum in the 21st century - that is commercial rocket flights. One driving factor was the first successful landing of the propulsion stage of SpaceX Falcon 9 rocket in 2015, thereby reducing the cost of a single launch. However, the exponential increase in space traffic has begun to cause significant greenhouse gas emissions [10]. Following in the footsteps of the aforementioned power engineering and aviation industries, here too we can expect the imposition of constraints in the future and thus new design challenges. Considering the probability of space launch failure, which was 5% in 2023 [11], it can be concluded that there is already a wide field for improvements. Part of the problem here is also related to thermal stresses, as rocket engines operate at temperatures in the order of 3,000 degrees Celsius. Design inadequacies can lead to serious failures such as rocket nozzle fractures [12], particularly in complex vertical landing conditions [13].

Industrial needs placing machines in new working conditions or requiring weight reduction, suggest that it is crucial to acquire techniques for predicting the strength and stability of these structures. The rapid development of computational methods in this direction has been initiated by the establishment of the foundations of the Finite Element Method (FEM) already in the 1940s. With regard to that event, the authors of the publication [Liu] refer to the current stage of knowledge of this methodology, which subjectively began in 2018, as 'state-of-the-art FEM technology for the current and future eras of FEM research'. This means no less than that it is now possible to use FEM for many complex, static and dynamic issues, i.e. thermal effects, cyclic fatigue, crack propagation or modal and frequency analyses. Analogous to the Computational Fluid Dynamics method using mainly Finite Volumes, at this stage we may be inclined to refer to the method using Finite Elements in dynamic calculations as Computational Solid Dynamics (CSD).

The sectors mentioned before, i.e. power engineering, aviation and space launch services, face a shared problem, which is largely the changing boundary conditions of structures caused by hot fluid flow. Thus, in order to simulate the behaviour of such structures in detail, a combination of FEM and Computational Fluid Mechanics is required, which is known as the Fluid-Structure Interaction (FSI) methodology. It is worth noting here that the word ‘Structure’ is sometimes used interchangeably with the word ‘Solid’ in the literature. However, in order to emphasise the separation from the mechanics of shell structures, in the following discussion it was decided to adhere to the less used version - ‘Solid’. The term FSI is applied to calculations in which there is an exchange of information - force, heat, momentum, displacement - between the structure and fluid domains. This exchange can take place via one-way coupling as well as two-way coupling. However, in order to address the rapid thermal loads described above, this dissertation chooses to focus on a type of this methodology called Thermal-FSI, in a fully coupled, dynamic variant.

As demonstrated later in this paper, the field of Thermal FSI does not yet appear to be adequately documented in the literature. There are deficiencies in terms of experimental verification and benchmarks, especially for the case of two-way, non-stationary coupling. These shortcomings are not obvious given the contemporary sophistication of FEM as well as CFD methods. It was therefore decided to spark a trend to fill this gap, with a possibly simple experiment. Nevertheless, an additional condition is imposed, consisting in the occurrence of a non-linear phenomenon such as buckling due to varying thermal loading in a given test. The ability to numerically capture that behaviour of the structure thus becomes a validation factor, right alongside heat transfer and linear deformation, giving Thermal FSI analysis the ability to demonstrate an advantage over other types of thermal analysis.

The choice of structure for analysis did not prove straightforward. This is because both measurement possibilities, thermal conditions and the actual occurrence of non-linear deflection had to be taken into account. Thus, the selected structure had to be characterised by:

- sufficiently rapid heat exchange between the fluid and the solid,
- the presence of repeatable buckling,
- measurement capabilities that do not interfere with fluid and solid behaviour,
- as low cost as possible, i.e. the availability of the selected materials and operation under conditions as close as possible to the environment.

A series of preliminary numerical analyses showed that the above features were hard to achieve for hot gas flows through relatively straight channels, e.g. through the formation of a wall layer, reducing heat transfer. A number of complex test stands were also developed, which in turn did not guarantee the occurrence of buckling. The final system that met all the requirements was an open thin-walled tank into which hot water was poured. This simple structure had been enclosed with a measuring rig so that the boundary conditions remained reproducible. It was then possible to reconstruct such a structure numerically and subject it not only to Thermal FSI analysis, but also to more common analyses such as Thermal Structural or Conjugated Heat Transfer, comparing the results.

1.2 Purpose and scope of work

Considering the industrial challenges described above and the current state of understanding of Thermal Fluid-Solid Interaction methodology, the aim of this dissertation is:

- To determine whether contemporary commercial numerical tools are suitable for simulating rapid, nonlinear thermal phenomena with Thermal-FSI method for industrial purposes.
- To compare and demonstrate the advantages and disadvantages of Thermal-FSI method against Thermal Structural and Conjugated Heat Transfer methods.

Therefore, in the first instance, Chapter 2 *Literature review* presents the literature items since the emergence of the term FSI. Applications, developmental issues and tools are discussed here, splitting the chapter into the more popular Momentum FSI type of analysis and the target Thermal FSI.

Then, Chapter 3 *Model theory* firstly presents the ideal FSI numerical model, and then discusses the models actually used in the Computational Fluid Dynamics and Computational Solid Dynamics solvers, for the target numerical analysis. Lastly, the coupling of the two solvers is discussed.

Chapter 4 *Experimental stand - a steel thin-walled container* provides a detailed presentation of the structure chosen for analysis as well as the experimental stand. It then presents the results of the measurements, in the form of temperature and displacement curves at selected points, supplemented by photographs of the water flow.

In Chapter 5 *Coupled Thermal-FSI numerical analysis*, the heart of this dissertation, the focus is on the target analysis of Thermal FSI, as well as the comparative Thermal Structural and Conjugated Heat Transfer. First, a simple mesh density analysis was performed for the fluid domain. This was followed by a description of boundary conditions, material data as well as CFD and CSD solver settings. Finally, a range of results for the three types of analysis is presented, comparing them to experimental results. Differences in the results of stress calculations are also considered here.

Finally, Chapter 6 *Conclusions* briefly summarises each of the previous chapters. Furthermore, the results of the numerical analyses are discussed here and a comparison of deviations from the experimental results is presented. A number of observations on the Thermal FSI methodology are also detailed.

Chapter 2

Literature review

2.1 Momentum Fluid-Structure Interaction

The first references to fluid-structure interaction appear in the 1970s, mainly in the field of nuclear power. Specifically, the term "fluid-solid interaction" appears in a paper from researchers Krajcinovic D. and Carey J. [14] and refers to an analytical model of the interaction of reactor core elements with the surrounding coolant. In this work, pipeline vibrations were reduced to a nonlinear differential equation describing the motion of an oscillator. Another pair of researchers, like the previous one working in the US, Illinois, in a publication [15] focused on the safety transient analysis of reactor containment structures, using FEM with fluid and solid elements. This approach led a year later to a review of the numerical FSI methods methods of that time by Belytschko T. [16]. The author pointed out the shortcomings of the available programs, i.e., consideration of compressible fluids or three-dimensional approach, needed for comprehensive analyses.

Considering that the above mentioned studies were mainly based on the exchange of momentum between a fluid and a solid, they can currently be secioned off to the Momentum-FSI field. Since then, the development of this branch has dynamically accelerated in terms of evolving numerical tools as well as in terms of finding applications in other fields of science. Modern numerical analyses often combine momentum exchange with heat transfer and other phenomena, which will be elaborated later. Today, FSI analysis is possible using not only in-house programs, but also commercial software and open-source code. Thus, based on the 1977 experiment [17], the authors of the publication [18] performed a benchmark study of momentum-FSI analysis using commercial computational solvers, i.e. LS-Dyna ALE, LS-Dyna ICFD, ANSYS CFX and Star-CCM+/ABAQUS. The results obtained from simulating the impact of water on the offshore structure gave rough convergence with experiment and relatively small discrepancies in the results, but also showed sensitivity to computational methods and meshing. In the meantime, there was a need to develop a benchmark experiment that was more oriented toward validating FSI models. The widely cited proposal by Turek S. and Hron J. [19], involving laminar flow around an elastic object which results in self-induced oscillations, stood out here. This proposal was used, among others, in the work of [20], where a good validation of the solver for FSI analysis ModsFsiFoam, based on the open-source OpenFoam software, was obtained. A similar experimental approach can be referenced within paper of Ziółkowski et al. [21], where a thin metal sheet was placed in a wind tunnel. Thus, a plot of its oscillations and maximum deformations was provided. Moreover, fairly good convergence was obtained using only numerical one-way FSI analysis, i.e., transferring only the pressure field from the CFD solver to the FEA solver. For structures characterized by regularity, approaches that simplify a given physical system are still used. For example, in the work [22], a one-dimensional system of FSI equations was used to determine pressure oscillations in the pipeline, due to the waterhammer phenomenon. The results emphasize the importance of selecting the parameters of viscoelastic pipe support.

The aforementioned tools for numerical Momentum FSI analysis, which are often still under development, can already find many applications in industrial issues. In the case of frequency analysis, in addition to pipeline studies, the FSI approach is proving useful in wide-area power engineering sector. A case in point is the publication of Ullah H. et al [23], where this type of analysis was performed using ANSYS software for a horizontal tidal current turbine. In addition to the fatigue results of the structure, authors also determined its modal frequencies and verified that the turbine operated away from its natural frequencies. In turn, in the publication [24], FSI analysis was used to investigate an innovative method of gust energy harvesting in an aircraft wing. The results provided information on the relationship of inflowing air to the power generated by the harvesters. In addition, the study utilized the coupling of CFD and CSD solvers using a method of optimized data exchange between computational cores. According to the authors, this method reduced computation time compared to ANSYS software by 87%. Numerical analysis of FSI can also be successfully adapted for more precise applications. A good example of this is the article [25], where the subject of the authors' study was an water-lubricated, double-liner bearing. The system analysed consisted of a rotating shaft, a water film, a first and a second liner. By varying the shaft speed and thickness of the individual liners, a number of operational and design conclusions were obtained through the resulting friction coefficients, stresses and deformations. It is worth mentioning that numerical analyses of FSIs are also gaining popularity in the medical industry, especially when it comes to the interaction of the blood pumped by the heart with the walls of blood vessels, as in the publication [26]. The authors succeeded in verifying with a real study the results of the analysis carried out with ANSYS software and located various mechanical factors that could endanger the patient's health.

2.2 Thermal Fluid-Structure Interaction

If to the coupling of fluid and structure by the momentum equation a heat exchange is added, then the coupling called Thermal FSI is obtained. However, in some cases the set of equations can be simplified. For example, in publication [27], the authors undertook a one-way 2D Thermal FSI analysis of an accelerated steam turbine start-up with cooling steam injection. As the thermal stresses present in this case far exceeded those derived from the steam pressure, the momentum transfer through the FSI could be neglected. Simultaneously, the momentum equation for the fluid itself was fully retained. It can be stated that this type of simplification reduces the Thermal FSI analysis to a Conjugated Heat Transfer analysis with the calculation of thermal stresses. An interesting development of FSI heat transfer methods can be found in works of Hassanjanikhoshkroud [28, 29]. The author, based on a simplified model of fluid flowing through hot rocks, applied thermo-hydro-mechanical coupling using a fictitious domain method. Further, another development of FSI heat transfer is proposed by Badur et al [30]. In this publication, the authors introduce a thin but finite thermal layer between a fluid and a solid, defined as the Smoluchowski thermal length jump. This approach modifies the interaction of the two media with the energy equation, undermining the need to derive experimental Nusselt and Stanton numbers. Another significant contribution to the development of Thermal FSI analysis is marked by a PhD thesis by Pironkov [31]. The aim of the thesis was to develop and implement a full-coupling framework using an in-house code for flow and the open-source FEAP code for solids linked by the MpCCI interface. The framework was validated, and then based on several examples from the literature, numerical analyses were performed in terms of different grid dislocation methods, turbulence models or convergence. The work also includes a valuable theoretical review regarding Thermal FSI equations and calculation schemes.

Referring to the experimental verification of Thermal FSI models, the literature resources are relatively limited. In benchmark terms, the publication [32] shows the approach of placing a heated plate in a wind tunnel. While in the numerical analysis performed, the correlation of the fluid velocity field with the slab temperature is noted, the need for a more thorough verification of the assumptions is indicated. A similar approach was used in the work of Willems S. et al [33], where flat and curved heated panels made of fibre-reinforced ceramics were investigated in a wind tunnel with hipersonic flows. A complex numerical analysis, taking into account radiation and catalytic chemical reactions, was carried out using the CFD solver DLR TAU and the FEM solver ANSYS. This provided a better insight into the physical phenomena occurring in the panel at temperatures above 1000°C and highlighted the advantages of non-stationary 3D analysis. Another, more specific example might be experimental validation of the Thermal FSI model for face seals of nuclear reactor coolant pumps presented in a publication by Huang W. et al. [34]. The value measured experimentally was the leakage intensity in the differential pressure function. Numerical analysis was performed on the basis of the finite element method for both the solid and the fluid, obtaining a good convergence of results with experiment. The dependence of the mechanical stresses on the thermal stresses under varying pump modes was thus determined. Another specific approach to the experimental validation of Thermal FSI is presented in Dhar S. et al [35], focusing on external gear machines. In this case, the measured experimental value was lateral gap leakage, dependent on absolute lubricating film thickness. For the multi-physics and multi-domain numerical analysis, a number of solvers were used, including OpenFoam as well as in-house code. Analysing lateral lubricating gaps between gears and lateral bushes, a good convergence with experiment was also obtained. The work showed that the implemented coupled Thermal FSI model better predicted the thickness of the lubricating film in certain gear operating ranges, compared to an isothermal analysis.

Numerical Thermal FSI analyses have now found their way into wide-ranging applications in thermal power engineering, particularly in one-way form. An example of this is the publication [36], where the author performed a numerical analysis of steam flow through a steel Y-pipe with time-varying parameters in the context of accelerated power plant start-up. This yielded the varying mechanical and thermal hoop stresses of the pipeline element, detailing the operating points for their maximum values. In terms of stress determination, Burzynski's strength hypothesis [37] is worth mentioning. As it is characterised by the additional consideration of the effect of temperature, this makes it an important addition to the Thermal FSI framework. A comparison of the most popular Huber-Mises-Hencky strain hypothesis with Burzynski's hypothesis for thermal load of turbine blades can be found in papers [38, 39]. Thermal FSI numerical analyses are also used in predicting the consequences of accidents. For example, in the work of Nariman N. A. [40], an analysis of various bridge fire scenarios was performed taking into account lateral winds as well as vibration and stress. Further, in the publication by Franci A. et al [41], the subject of analysis was the course of failure of a nuclear reactor in the form of a meltdown of its core. The authors, using the Lagrangian framework of Particle Finite Element Method, took into account the phase transition of the nuclear fuel with its flow and associated thermal effects. However, the full potential of the numerical analysis of Thermal FSI was presented in the work of Joo H. et al [42]. The object of study in this case was the deformation of the closure aft inside a vertical rocket launcher. This deformation, resulted from the hot gas flow of the rocket and, at the same time, influenced gas dissipation inside the launcher.

The implemented co-rotational formulation was used for the analysis along with the level-set method, verifying it beforehand with the results of the commercial software ABAQS and ANSYS. The final results were used to select the design parameters of the closure afts that were optimal in terms of gas distribution. As can be seen, FSI modelling is characterised by a noticeable multidisciplinarity. General insight in this regard is provided by a review by Ochrymiuk T. et al [43], where, depending on the type of coupling, in addition to Momentum and Thermal FSI, examples of Mass FSI, Electrical FSI and Biological FSI are given.

Chapter 3

Model theory

3.1 General model of Fluid-Solid Interaction

Considering the situation in which the fluid comes into contact with a solid, there can be defined the contact surface Ω_{FSI}, which represents all bounary parameters. Under non-stationary conditions, in the area under analysis or in the numerical cell, fluid and solid have their instantaneous volumes ∂V_F and ∂V_S. Inside these volumes, there can be defined vectors $\mathbf{n}_F$, $\mathbf{n}_S$ normal to the surface Ω_{FSI} as shown in Fig. 3.1. In addition, due to forces, thermal expansion or forced motion, the contact surface moves in the normal direction with the displacement velocity vector $\mathbf{v}_\Omega$. Ultimately, the following conditions are met at the contact surface:

$$\mathbf{v}_\Omega = \mathbf{v}_{Fluid} = \mathbf{v}_{Solid}, \tag{3.1}$$

$$\mathbf{n}_F = -\mathbf{n}_S. \tag{3.2}$$

In the terms of numerical analisys, both the fluid and solid domain must be subdivided according to Finite Volume Methods (FVM) or Finite Element Method (FEM). However, for each continuum following quantities can be determined: density of the continuum ρ, velocity vector $\mathbf{v}\left(\mathbf{x}, t\right)$ and vector of

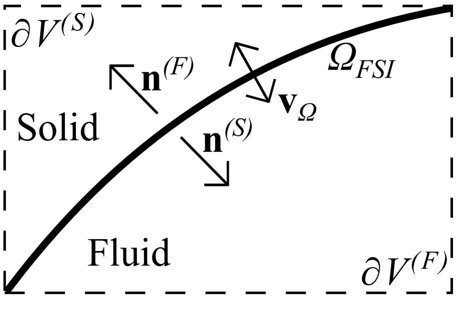

Figure 3.1: Fluid - solid interface

total heat flux $\mathbf{q}_t$. Total heat flux may consist of several terms depending on the case and scale, such as molecular heat flux $\mathbf{q}$, turbulent heat flux $\mathbf{q}_{turb}$ and radiation heat flux $\mathbf{q}_{rad}$:

$$\mathbf{q}_T = \mathbf{q} + \mathbf{q}_{turb} + \mathbf{q}_{rad} + \dots \tag{3.3}$$

Considering the mathematical models on the fluid side first, it is necessary to adhere to the basic conservation equations of Computational Fluid Dynamics in differential form, valid for every finite volume grid cell [44]:

- mass conservation equation;

$$\frac{\partial \rho}{\partial t} + \operatorname{div}(\rho \mathbf{v}) = 0 \quad , \tag{3.4}$$

- momentum conservation equation

$$\frac{\partial}{\partial t}(\rho \mathbf{v}) + \operatorname{div}(\rho \mathbf{v} \otimes \mathbf{v}) = \operatorname{div}(\mathbf{T}) + \rho \mathbf{f} \quad , \tag{3.5}$$

- energy conservation equation;

$$\frac{\partial}{\partial t}(\rho e) + \operatorname{div}(\rho e \mathbf{v} - \mathbf{q}_T) = \operatorname{div}(\mathbf{T} \cdot \mathbf{v}) + \rho \mathbf{f} \cdot \mathbf{v} \quad , \tag{3.6}$$

where p is the hydrostatic pressure, $\mathbf{I}$ is the unit tensor, $\mathbf{T}$ is the molecular tensor of total viscous stresses, and $\mathbf{f}$ is the vector of external force. The total energy e consists of internal unit energy u end kinetic energy as follows:

$$e = u + \frac{1}{2}\mathbf{v}^2 \quad . \tag{3.7}$$

In the above equations of conservation, beginning with the equation of conservation of mass, the term $\partial\rho/\partial t$ represents the local change in density of the fluid over time. Then term $\operatorname{div}(\rho \mathbf{v})$ describes the distribution of mass convective (that is transported by the flow) flux in the directions of the coordinate system. In the equation of conservation of momentum, the first term $\partial/\partial t(\rho \mathbf{v})$ accounts for the local change in momentum over time, and the term $\operatorname{div}(\rho \mathbf{v} \otimes \mathbf{v})$ is responsible for the distribution of convective momentum fluxes in the cell. Then, the expression $\operatorname{div}(\mathbf{T})$ follows from the fact of the presence of the stresses at the boundary of the volume V_F, described by the tensor $\mathbf{T}$:

$$\mathbf{T} = -p\mathbf{I} + \boldsymbol{\tau} \quad , \tag{3.8}$$

where $-p\mathbf{I}$ is the isotropic pressure component and $\boldsymbol{\tau}$ is the viscous shear stress tensor. Finally, $\rho \mathbf{f}$ represents the sum of external volumetric forces per unit volume. Turning to the equation of conservation of energy, the first term $\partial/\partial t\,(\rho e)$ represents the local change of total energy over time. The next expression involves the divergence of two phenomena, where $\rho e\mathbf{v}$ is the convective flux of energy and $\mathbf{q}_T$ is responsible for describing the diffusion of heat in the fluid at rest under Furier's law. Next, the component $\mathbf{T}\cdot\mathbf{v}$ defines the surface sources, resulting from the work done on the fluid by internal shear stresses, and the component $\rho\mathbf{f}\cdot\mathbf{v}$ represents the energy resulting from external forces.

Let it be assumed for the purposes of theoretical considerations that the solid body is also discretized using the FVM. In this case, taking into account its dynamics, deformation and phase transformations, it is possible to prepare a system of equations based on the CFD equations. Thus, it is possible to obtain [45, 46]:

- mass conservation equation;

$$\frac{\partial}{\partial t}(\rho) + \operatorname{div}(\rho\mathbf{v}) = 0 \quad , \tag{3.9}$$

- momentum conservation equation;

$$\frac{\partial}{\partial t}(\rho\mathbf{v}) + \operatorname{div}(\rho\mathbf{v}\otimes\mathbf{v}) = \operatorname{div}(\boldsymbol{\sigma}) + \rho\mathbf{f} \quad , \tag{3.10}$$

- energy conservation equation;

$$\frac{\partial}{\partial t}(\rho e) + \operatorname{div}(\rho e\mathbf{v} - \mathbf{q}_T) = \operatorname{div}(\boldsymbol{\sigma}\cdot\mathbf{v}) + \rho\mathbf{f}\cdot\mathbf{v} \quad , \tag{3.11}$$

where $\boldsymbol{\sigma}$ is the mechanical stresses tensor. This tensor is subject to decomposition into a principal part $\boldsymbol{\sigma}_0$ and a deviator part $\boldsymbol{\sigma}_d$:

$$\boldsymbol{\sigma} = \boldsymbol{\sigma}_0 + \boldsymbol{\sigma}_d = \begin{bmatrix} \sigma_0 & 0 & 0 \\ 0 & \sigma_0 & 0 \\ 0 & 0 & \sigma_0 \end{bmatrix} + \begin{bmatrix} \sigma_x - \sigma_0 & \tau_{xy} & \tau_{xz} \\ \tau_{yx} & \sigma_y - \sigma_0 & \tau_{yz} \\ \tau_{zx} & \tau_{zy} & \sigma_z - \sigma_0 \end{bmatrix} \tag{3.12}$$

Where σ stands for the normal stress component, and τ for the tangential stress component, with the average normal stress σ_0 :

$$\sigma_0 = \frac{1}{3}(\sigma_x + \sigma_y + \sigma_z) \quad . \tag{3.13}$$

The above equations of conservation of mass, momentum and energy for CFD and CSD were written in a form highlighting fluxes and sources, following the formula of the general equation for a scalar quantity per unit volume $\mathcal{U}$ suggested by Hirsh [44].

$$\frac{\partial}{\partial t}\mathcal{U} + \operatorname{div}(\mathcal{F}_c + \mathcal{F}_d) = \operatorname{div}(\mathcal{S}_s) + \mathcal{S}_v \quad . \tag{3.14}$$

Individual expressions appearing in eq. 3.14 can be described as:
change in density of an intense variable over time;

$$\frac{\partial}{\partial t}\mathcal{U} = \begin{Bmatrix} \partial_t \rho \\ \partial_t \left(\rho \mathbf{v}\right) \\ \partial_t \left(\rho e\right) \end{Bmatrix} \quad , \tag{3.15}$$

convective flux through surfaces limiting the volume;

$$\mathcal{F}_c = \begin{Bmatrix} \rho \mathbf{v} \\ \rho \mathbf{v} \otimes \mathbf{v} \\ \rho e \mathbf{v} \end{Bmatrix} \quad , \tag{3.16}$$

diffusive flux through surfaces limiting the volume;

$$\mathcal{F}_d = \begin{Bmatrix} 0 \\ 0 \\ -\mathbf{q}_T \end{Bmatrix} \quad , \tag{3.17}$$

surface sources - different for fluid (F) and solid (S);

$$\mathcal{S}_s^{(F)} = \begin{Bmatrix} 0 \\ -p\mathbf{I} + \boldsymbol{\tau} \\ -p\mathbf{v} + \boldsymbol{\tau} \cdot \mathbf{v} \end{Bmatrix}, \quad \mathcal{S}_s^{(S)} = \begin{Bmatrix} 0 \\ \boldsymbol{\sigma}_0 + \boldsymbol{\sigma}_d \\ \boldsymbol{\sigma}_0 \cdot \mathbf{v} + \boldsymbol{\sigma}_d \cdot \mathbf{v} \end{Bmatrix} \quad , \tag{3.18}$$

volumetric sources;

$$\mathcal{S}_v = \begin{Bmatrix} 0 \\ \rho \mathbf{f} \\ \rho \mathbf{f} \cdot \mathbf{v} \end{Bmatrix} \quad . \tag{3.19}$$

Individual fluxes describe the flow of a given quantity across the boundaries of a finite volume in directions normal to its surface. Sources, on the other hand, describe the generation or disappearance of that quantity at the cell surface or in the volume. Taking the conservation of momentum equation as an example, the surface source is the stresses arising from the vicinity of other cells, and the volume source is an external force acting on the entire volume of the cell, such as gravitational force. However, in order to transparently describe the fluxes exchanged by the FSI interface Ω_{FSI}, it is necessary to separate one more flux from the surface source - the elastic flux $\mathcal{F}_e$. With reference to the above conservation equations, it takes the form of:

$$\mathcal{F}_e^{(F)} = \begin{Bmatrix} 0 \\ -p\mathbf{I} \\ -p\mathbf{v} \end{Bmatrix}, \quad \mathcal{F}_e^{(S)} = \begin{Bmatrix} 0 \\ \boldsymbol{\sigma}_0 \\ \boldsymbol{\sigma}_0 \cdot \mathbf{v} \end{Bmatrix} \quad , \tag{3.20}$$

The presence of elastic flux is responsible for exerting a force on the boundary surface, for example, in the case of a closed pressure vessel. Transferring the new flux to the divergence on the left side of the eq 3.14 and remaining the deviatoric parts of the stress tensors as surface sources gives:

$$\frac{\partial}{\partial t}\mathcal{U} + \operatorname{div}\left(\mathcal{F}_c + \mathcal{F}_d - \mathcal{F}_e\right) = \operatorname{div}\left(\mathcal{S}_s\right) + \mathcal{S}_v \quad . \tag{3.21}$$

Considering that only fluxes cross finite volume boundaries, they must also be preserved properly when crossing a fluid-solid boundary. As this transfer takes place in the normal direction, the following relationship that takes into account the total sum of the fluxes $\mathcal{F}$ must be met:

$$\mathcal{F}^{(F)} \cdot \mathbf{n}^{(F)} = \mathcal{F}^{(S)} \cdot \mathbf{n}^{(S)}. \tag{3.22}$$

Referring to the above, there can be defined three following balance equations for FSI interface:

- transfer of mass flux;

$$\left(\rho^{(F)}\mathbf{v}^{(F)}\right) \cdot \mathbf{n}^{(F)} = \left(\rho^{(S)}\mathbf{v}^{(S)}\right) \cdot \mathbf{n}^{(S)} \quad , \tag{3.23}$$

- transfer of momentum flux;

$$\left(\rho^{(F)}\mathbf{v}^{(F)} \otimes \mathbf{v}^{(F)} + p\mathbf{I}\right) \cdot \mathbf{n}^{(F)} = \left(\rho^{(S)}\mathbf{v}^{(S)} \otimes \mathbf{v}^{(S)} - \boldsymbol{\sigma}_0\right) \cdot \mathbf{n}^{(S)} \quad , \tag{3.24}$$

- transfer of energy flux;

$$\left(\rho^{(F)}e^{(F)}\mathbf{v}^{(F)} - \mathbf{q}_T + p\mathbf{v}^{(F)}\right) \cdot \mathbf{n}^{(F)} = \left(\rho^{(S)}e^{(S)}\mathbf{v}^{(S)} - \mathbf{q}_T - \boldsymbol{\sigma}_0\right) \cdot \mathbf{n}^{(S)} \quad , \tag{3.25}$$

In this way, a full description of the interaction between the fluid and the solid through the Ω_{FSI} surface was obtained. It is worth mentioning here that the mass transfer equation applies to rather specific cases, i.e. chemical reactions or phase transformations.

3.2 Case-specific model of Computational Fluid Dynamics

In order to model the flow of water in the container, it is necessary to take into account its inlet and also the outlet of the air pushed out by the water. This means calculating the two-phase flow. For this purpose, the Volume of Fluid model was used on the CFD solver side. An "Euler-Euler" model was also applied, in which the equations of both the fluid and the individual phases are calculated relative to a fixed coordinate system.

Defining the boundary between the phases is done by solving the volume fraction continuity equation for the water phase w [47, 48]:

$$\frac{1}{\rho_w}\left[\frac{\partial}{\partial t}\left(\alpha_w\rho_w\right) + \operatorname{div}\left(\alpha_w\rho_w\mathbf{v}_w\right) = \dot{m}_{aw} - \dot{m}_{wa}\right] \quad , \tag{3.26}$$

where α_w is the water's volume fraction, $\dot{m}_{aw}$ is the mass transfer through the cell boundary from the air phase to the water phase and $\dot{m}_{aw}$ from the water phase to the air phase. The air phase is computed directly from relationship:

$$\alpha_a = 1 - \alpha_w \quad . \tag{3.27}$$

To represent the boundary between the fluids in a single cell, a geometric reconstruction scheme [49] was used, which is based on a piecewise-linear approach. In the considered case, the Explicit Formulation method was used to solve the volume fraction continuity equation, where the water volume fraction is calculated for the current time n step based on values taken from the previous time step n [48]:

$$\frac{\alpha_w^n \rho_w^n - \alpha_w^{n-1} \rho_w^{n-1}}{\Delta t} + \sum_f \left(\rho_w \dot{V}_f^{n-1} \alpha_{w,f}^{n-1} \right) = \left(\dot{m}_{aw} - \dot{m}_{wa} \right) V \quad , \tag{3.28}$$

where f is a FVM cell face index, $\dot{V}_f^n$ is a volume flux through the face in the normal direction, $\alpha_{w,f}$ is a face value of the volume fraction and V is the cell volume. The presence of both phases in a single computational cell implies the necessity of proportional determination of fluid properties (density, viscosity, thermal conductivity, etc.). Thus, using the example of density, the relation is obtained:

$$\rho = \alpha_a \rho_a + \left(1 - \alpha_a\right) \rho_w \quad . \tag{3.29}$$

However, in the case of energy, its mass average is calculated:

$$E = \frac{\alpha_w \rho_w E_w + \alpha_a \rho_a E_a}{\alpha_w \rho_w + \alpha_a \rho_a} \quad , \tag{3.30}$$

where the energy of an individual phase, including the enthalpy of the fluid h and using water as an example, is:

$$E_w = u_w + \frac{v^2}{2} = h_w - \frac{p}{\rho_w} + \frac{v^2}{2} \quad . \tag{3.31}$$

The surface tension between the two phases of the fluid is represented by an additional volume force term in the momentum equation described as [48, 50]:

$$\boldsymbol{f}_\sigma = \sigma \frac{\rho \kappa_w \mathrm{grad} \alpha_w}{\frac{1}{2}(\rho_w + \rho_a)} \tag{3.32}$$

where σ is the surface tension coefficient and κ is the curvature of the phase boundary, defined as the divergence of the unit normal vector, $\kappa = \mathrm{div}\left(\mathbf{n}/|\mathbf{n}|\right)$. In the case under consideration, Thermal FSI modeling takes into account the thermal deformation of the solid. These cause wall motion and thus mesh motion in the fluid domain. The motion is taken into account using the Dynamic Mesh method. By analogy with the 3.14 equation, the general integral equation for any scalar ϕ in a volume V with moving boundaries can be represented as:

$$\frac{d}{dt}\int_V \rho\phi dV+\int_{\partial V}\rho\phi(\mathbf{v}-\mathbf{v}_m)\cdot d\mathbf{S}-\int_{\partial V}\mathit{\Gamma}\mathrm{grad}\phi\cdot d\mathbf{S}=\int_{\partial V}\mathcal{S}_s\cdot d\mathbf{S}+\int_V \mathcal{S}_v dV \quad , \tag{3.33}$$

where $d\mathbf{S}$ is the normal surface element vector, $\mathbf{v}_m$ is the velocity vector of the moving mesh and $\mathit{\Gamma}$ is the diffusion coefficient. Since First Order Implicit transient formulation was used in the calculation, with reference to the current time step n the first term of the above equation takes the form:

$$\frac{d}{dt}\int_V \rho\phi dV=\frac{(\rho\phi V)^{n+1}-(\rho\phi V)^n}{\Delta t} \quad . \tag{3.34}$$

Thus, the new cell volume is calculated as:

$$V^{n+1}=V^n+\frac{dV}{dt}\Delta t \quad . \tag{3.35}$$

In order to adequately represent the variety of flow phenomena occurring throughout the fluid domain, a flexible Baseline k-ω turbulence model extended with Shear Stress Transport was used, the basis of which are the equations:

$$\frac{\partial}{\partial t}(\rho k)+\mathrm{div}(\rho\mathbf{V}k)=\mathrm{div}(\mathit{\Gamma}_k\mathrm{grad}k)+G_k-Y_k+B_k \quad , \tag{3.36}$$

$$\frac{\partial}{\partial t}(\rho\omega)+\mathrm{div}(\rho\mathbf{V}\omega)=\mathrm{div}(\mathit{\Gamma}_\omega\mathrm{grad}\omega)+G_\omega-Y_\omega+B_\omega+D_\omega \quad . \tag{3.37}$$

Above, the turbulent kinetic energy is denoted by k, the specific dissipation rate by ω, and $\mathbf{V}$ is the velocity tensor. Then, in relation to k and ω, $\mathit{\Gamma}$ is the effective diffusivity, G denotes the property production, Y is the dissipation by turbulence and B refers to the buoyancy term. D_ω represents the cross-diffusion term.

3.3 Case-specific model of Computational Solid Dynamics

The purpose of CSD is to calculate deformation, stress as well as heat flow in a solid. It is worth noting here that the mechanical solver uses discretization via the Finite Element Method, in which, unlike the FVM, calculations are made relative to the element nodes, not its surface. In the case under consideration, mechanical as well as thermal loads are obtained through the FSI interface. The total deformation of the solid material $\boldsymbol{\varepsilon}$ in the elastic range consists of elastic $\boldsymbol{\varepsilon}_e$ and thermal $\boldsymbol{\varepsilon}_{th}$ strain tensors:

$$\boldsymbol{\varepsilon}=\boldsymbol{\varepsilon}_e+\boldsymbol{\varepsilon}_{th} \quad . \tag{3.38}$$

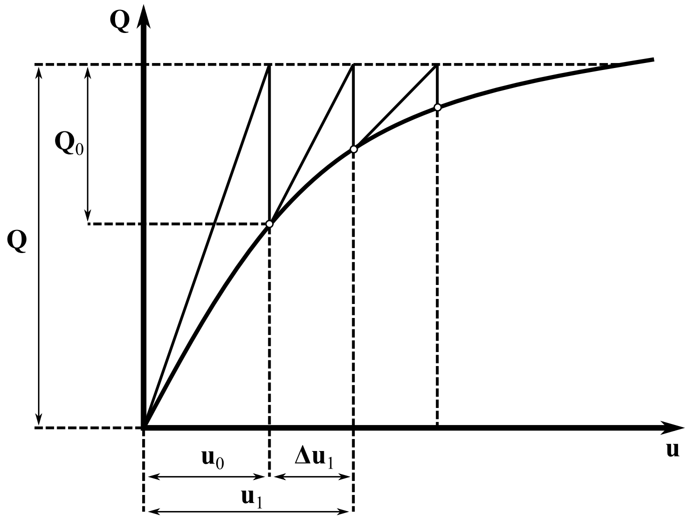

Figure 3.2: One-parameter interpretation of the Newton-Raphson iterative method

The thermal strain tensor is a result of the material's linear expansion with coefficient $\alpha(T)$ under temperature change:

$$\boldsymbol{\varepsilon}_{th} = \alpha\,(T - T_0)\,\mathbf{I}, \tag{3.39}$$

where T is the current local temperature, T_0 is a reference temperature, and $\mathbf{I}$ is the identity matrix, whereas the elastic strain tensor is the result of multiplying the strain-displacement matrix $\mathbf{B}$ with the nodal displacement vector $\mathbf{u}$:

$$\boldsymbol{\varepsilon}_e = \mathbf{B}\mathbf{u} \quad . \tag{3.40}$$

Through Hook's law, using elastic deformation and introducing the elasticity matrix $\mathbf{D}$, the stress tensor can be determined:

$$\boldsymbol{\sigma} = \mathbf{D}\boldsymbol{\varepsilon}_e \quad . \tag{3.41}$$

The nodal displacement vector is the basis of the equation of motion solved by the CSD solver within the transient dynamic analysis:

$$\mathbf{Q}(t) = \mathbf{M}\frac{\partial^2}{\partial t}\mathbf{u} + \mathbf{C}\frac{\partial}{\partial t}\mathbf{u} + \mathbf{K}\mathbf{u} \quad , \tag{3.42}$$

where $\mathbf{Q}(t)$ is the total load, $\mathbf{M}$ is the mass matrix, $\mathbf{C}$ is the damping matrix and $\mathbf{K}$ is the stiffness matrix. Solving nonlinear and transient numerical analyzes requires the use of appropriate iterative methods. In this case, the Newton-Raphson method illustrated in Fig. 3.2 was used.

By determining the increase of the generalized displacement as $\triangle\mathbf{u}$ and the linear stiffness matrix as $\mathbf{K}^L$, the initial displacement is obtained:

$$\mathbf{u}_0 = \left(\mathbf{K}^L\right)^{-1}\mathbf{Q}, \tag{3.43}$$

On the basis of $\mathbf{u}_0$, the stiffness increase from non-linearity $\mathbf{K}_0^{NL}$ is determined, which makes it possible to obtain a total stiffness matrix:

$$\mathbf{K} = \mathbf{K}^L + \mathbf{K}_0^{NL}. \tag{3.44}$$

The deformation state $\mathbf{u}_0$ is different from the real state, while the internal forces do not balance the load $\mathbf{Q}$, which gives an unbalanced load in the form:

$$\mathbf{Q}_0 = \left(\mathbf{K}^L + \mathbf{K}_0^{NL}\right)\mathbf{u}_0 - \mathbf{Q}, \tag{3.45}$$

which in turn is the source of additional displacements:

$$\triangle\mathbf{u}_1 = \left(\mathbf{K}^L + \mathbf{K}_0^{NL}\right)^{-1}\mathbf{Q}_0, \tag{3.46}$$

creating a new displacement state:

$$\mathbf{u}_1 = \mathbf{u}_0 + \triangle\mathbf{u}_1, \tag{3.47}$$

deviating from the actual state less than $\mathbf{u}_0$. This difference decreases with each i-th iteration at which $i-1$ iteration $\mathbf{u}_i$ is obtained.

3.4 Coupling of numerical solvers

The coupled thermal FSI analysis was performed using a package from ANSYS Inc. ANSYS Fluent was used as the CFD solver, and ANSYS Mechanical APDL in the form of the Transient Structural module was used as the CSD solver. In order to be able to perform simultaneous mechanical and thermal analysis in the mechanical solver, it was necessary to enforce the use of Type 226 elements supporting both analyses. The ANSYS System Coupling module was responsible for coupling the two solvers. It controls the exchange of information through the FSI interface, and is also responsible for mapping the surfaces and elements of the CFD and CSD meshes. In the case under consideration, no interpolation was required, since both meshes were separated from the structural discretization of the entire computational domain. Thus, 100% coverage of nodes at the FSI interface was achieved.

In practice, the transfer of quantities between solvers is quite simplistic, compared to the ideal case described in Section 3.1. For Thermal FSI analysis, three variables are transmitted from the CFD solver side: force, near wall temperature and heat transfer coefficient, while two variables are transmitted from the CSD solver side: temperature and mesh displacement.

Therefore a third iterative process, divided into coupling steps, is attached to the iterative processes of the two solvers, the convergence of which is based on the exchange of data through the FSI interface. In addition, each coupling step consists of a certain number of iterations. Achievement of coupling step convergence takes place after a preset minimum number of iterations have

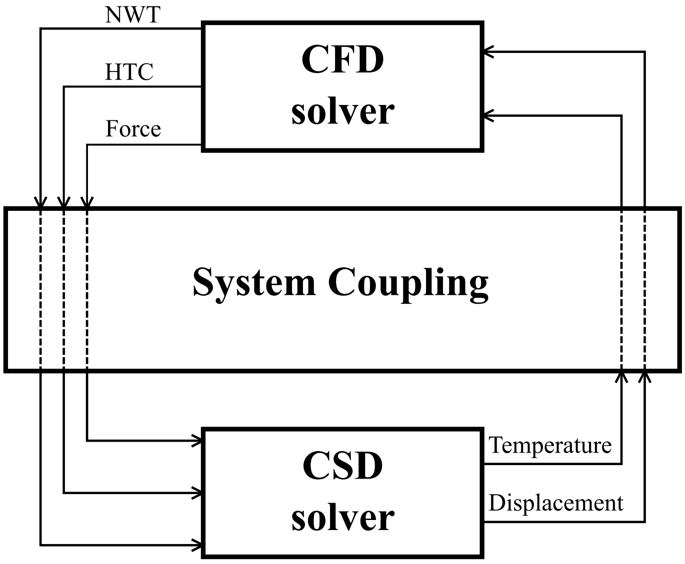

Figure 3.3: Scheme od coupled system; NWT - nwar wall temperature, HTC - heat transfer coefficient

been executed and the data exchange residuals have reached a defined level. The time step defined for the coupling step, is simultaneously the physical time step for both solvers - this is a certain limitation, due to the frequent discrepancy between the intensity of flow and mechanical phenomena. The start of each coupling iteration begins with the transfer of current data to the CSD solver - the initialization values or those calculated in the previous iteration. The internal iterative process of the CSD solver then begins. After recalculation, the updated values of temperature and mesh deformation are passed through FSI interface, starting an internal iterative process of the CFD solver with new boundary conditions. Achieving convergence of the CFD solver ends the coupling system iteration. Then the conditions for achieving coupled step convergence are checked - if they are not met, the next coupled iteration begins.

Chapter 4

Experimental stand - a steel thin-walled container

4.1 Experimental setup

Experimental studies of thermal nonlinear deformation were carried out on an example object, which was an open thin-walled container. It was made of ANSI 201 stainless steel with a sheet thickness of 0.7 mm. The experiment involved applying hot water to the center of the bottom of the tank using a tube. The stand was designed to make numerical reproduction of the object under study relatively simple. A schematic of the computationally relevant geometry is shown in Fig. 4.1.

During water dispensing, the vertical displacement in the middle of the bottom was measured, as well as the temperature of the bottom of the tank (point P1 and P2), the inlet water (point T3), and the environment. The distribution of thermocouples on the object of study is shown in Fig. 4.3. Measuring the temperature on the outside of the tank at point P1 provided information on vertical heat conduction in the steel, while point P2, 80 mm away along the shorter side, provided information on both vertical and horizontal heat conduction, depending on the water spread. In this way, the measurement was carried out 10 times. After each application of hot water, the container was dried and brought to ambient temperature. Since the observed deformation occurred in the form of rapid buckling of the bottom, it was important to leave both the bottom and side walls of the tank free. Thus, the tested structure was fixed only at the top edge, the implementation of which is shown in Fig. 4.2.

4.2 Measurement apparatus

A water presence sensor was installed at the operating inlet. It provided a binary signal that was transmitted both to the data acquisition system

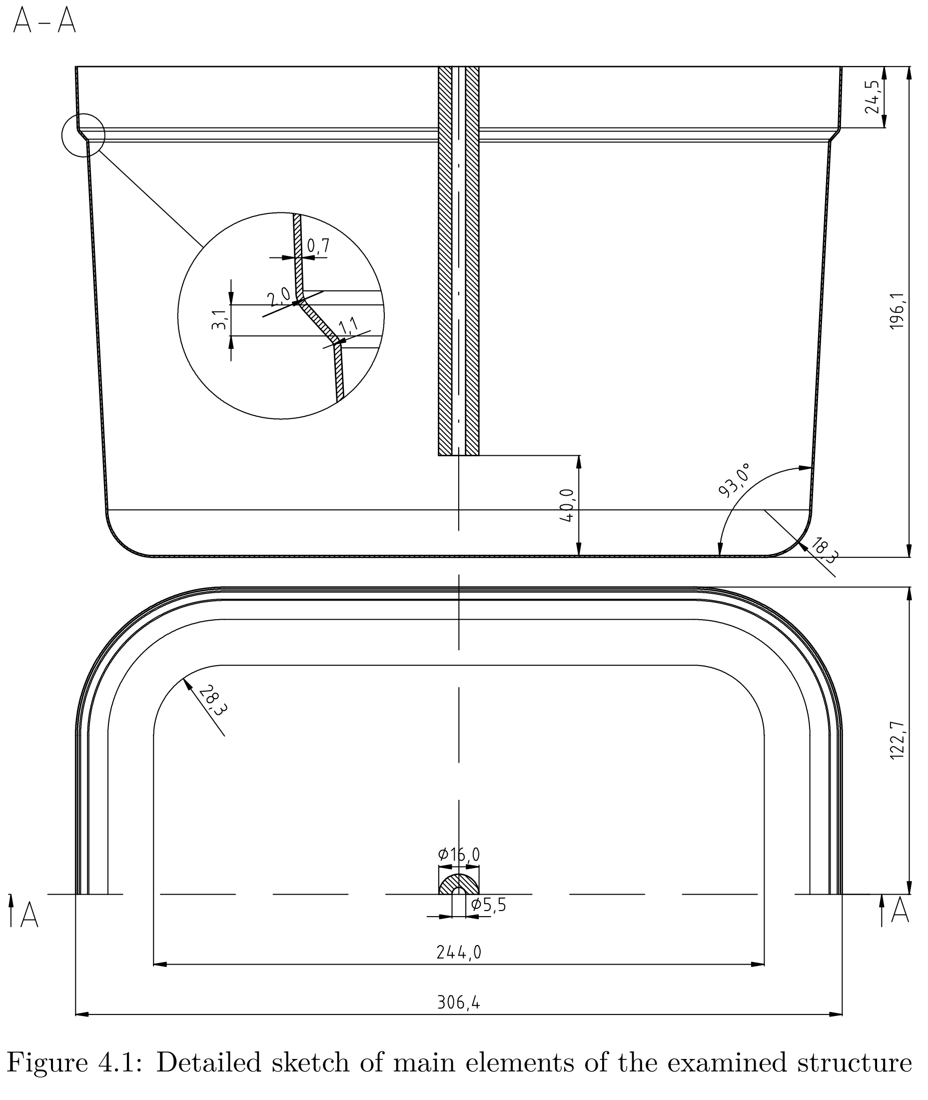

Figure 4.1: Detailed sketch of main elements of the examined structure

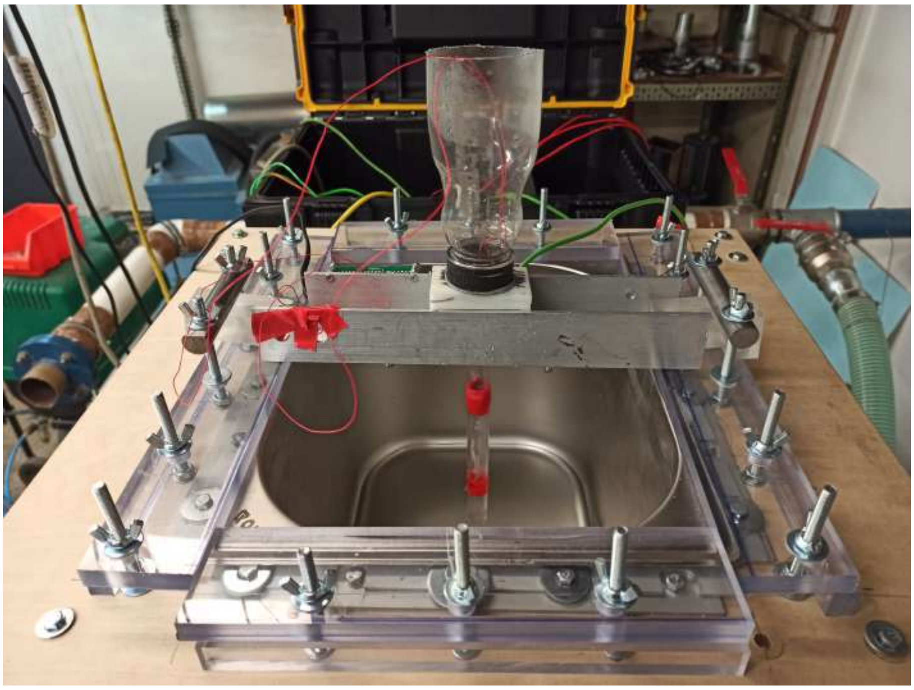

Figure 4.2: Photo of the experimental stand - view of the water feeder and container fixing

and to the light diodes - this made it possible to synchronize in time the signals from the thermocouples with the visual displacement measurement. The main measurement loop was timed to 100 Hz and it was triggered with a hardware synchronization signal. The time shift (uncertainty) between the synchronization signal and the first temperature measurement was not greater than 0.01 s. To attain a fast temperature response, the thermocouple K-type sensors with 0.5 mm shield diameter were used. All thermocouples were calibrated and verified prior to conducting the measurements. The procedure was done with the DRUCK DB-150 (GE-Sensing, Billerica, MA, USA) temperature calibrator. The reference temperature was supplied by PT100 ISOTECH (Isothermal Technology Ltd., Southport, UK) temperature transducer. The obtained precision (the value of the maximum error of the temperature value) readings from thermocouples was 0.1°C for 20°C and 0.15°C for 60°C. The accuracy of the temperature change measurement was better than 0.05°C in the whole temperature range of interest (between 20°C and 95°C). The measurements were taken using the NI cRIO9030 unit (with 9214 TC transducer module). When a stable temperature of 25°C is assured, the accuracy of internal clock is 40 ppp. It results in the relative error of time between subsequent measurements not greater than 0.00004, making this source of uncertainty negligible.

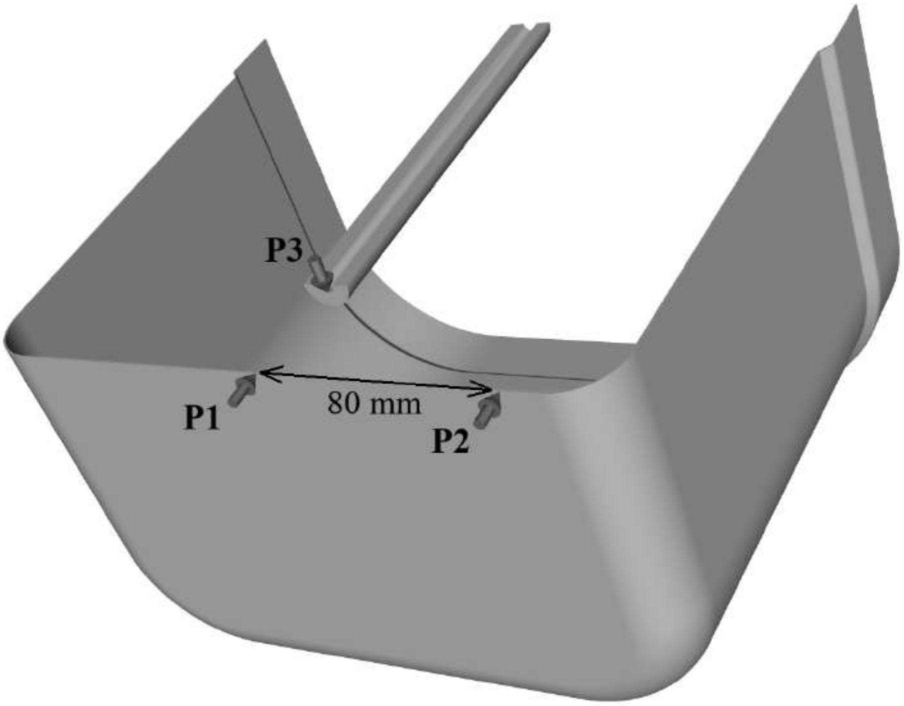

Figure 4.3: Placement of the temperature sensors

The detection of the container bottom position was done using the image analysis based on correlation. Images were taken with a FASTEC HiSPEC high-speed camera with Nikkor 286551 lens, as shown in Fig. 4.4. The final result was trunctuated to 1 pixel of resolution, resulting in +/- 0.5 pixel precision. This value corresponds to the 0.06 mm in real (laboratory) system of coordinates. Thus, if the change in position was less than 1 pixel, the displacement could not be recorded. For the frequency used in our measurements (500 frames per second) the maximum relative error of time between frames is less than 0.025%, making this a negligible source of uncertainty.

4.3 Results of the experiment

A total of 10 hot water spill tests were performed. Each of these tests resulted in rapid buckling of the bottom of the container. The average inlet temperature of the water (point T3) was 95°C with an average ambient temperature of 23.1°C. The recording time of the single measurement has been specified at 5 seconds. In each attempt, it was possible to distinguish 3 characteristic moments, as shown in the photos in Fig. 4.5: the flow of water with the vortex formed, the filling of the bottom and the ejection of water

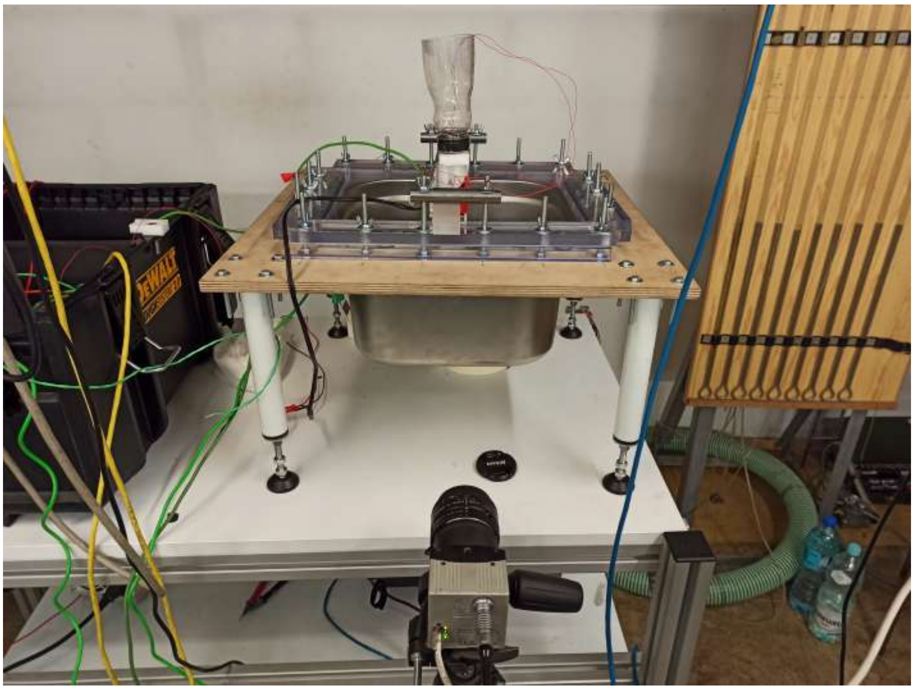

Figure 4.4: Photo of the experimental stand - side view of the container and high-speed camera

droplets due to rapid buckling.

The resulting temperature plots for a thermocouple located at the center of the bottom, on the outer side of the container (point P1) are shown in Fig. 4.6. The highest temperature spread between measurements was 6.92°C and occurred at a time of 0.39 s. Subsequently, temperature plots for a thermocouple offset from the center by 80 mm along the shorter side of the container (point P2), are shown in Fig. 4.7. In this case, the maximum temperature spread was 24.14°C for a measurement time of 1.80 s. Taking into account the temperature measurement accuracy of +/- 0.05 and negligible time measurement uncertainty, the total spread of temperature measurements for both thermocouples is shown in Fig. 4.8 and Fig. 4.9. In addition, the steel temperature range in Fig. 4.8 is paired with the averaged temperature of the water exiting the tube (point P3), which in turn will be used as the inlet boundary condition in the CFD analysis.

Meanwhile, the measurements of the vertical displacement of the bottom of the tank at point P1, resulting from thermal expansion, is shown in Fig. 4.10. In each case, four stages of bottom movement were observed: upward deformation, downward deformation, buckling jump and slow upward deformation. For all measurements, the maximum upward displacement was in the range from 3.48 mm to 3.96 mm, and the minimum downward

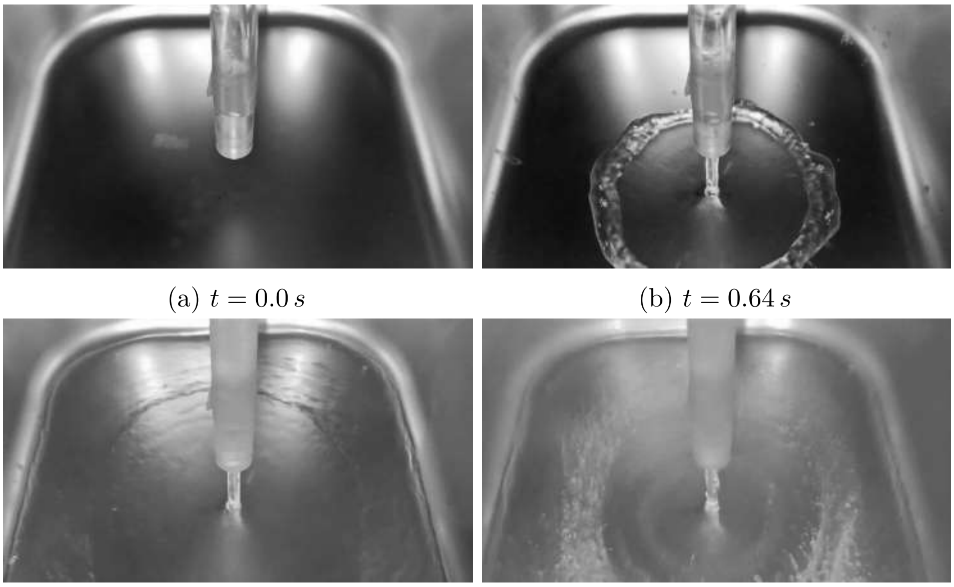

(a) $t = 0.0\,s$

(b) $t = 0.64\,s$

(c) $t = 2.53\,s$

(d) $t = 3.19\,s$

Figure 4.5: Water distribution in the container during the experiment

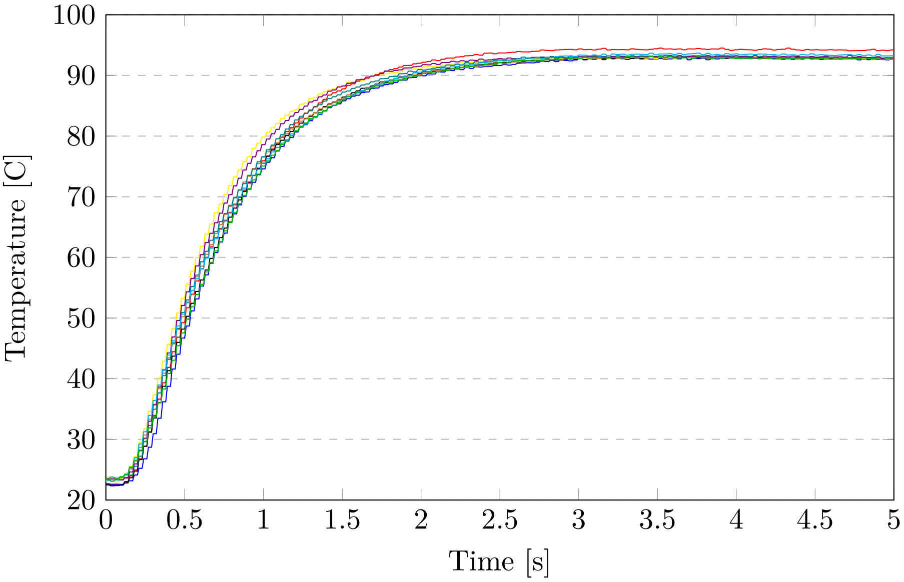

Figure 4.6: Temperature of the bottom at point P1

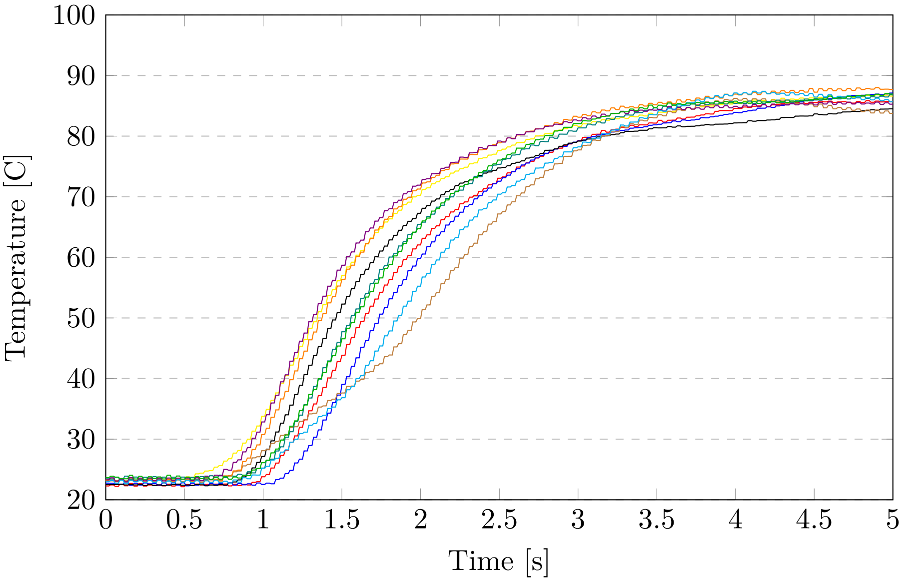

Figure 4.7: Temperature of the bottom at point P2

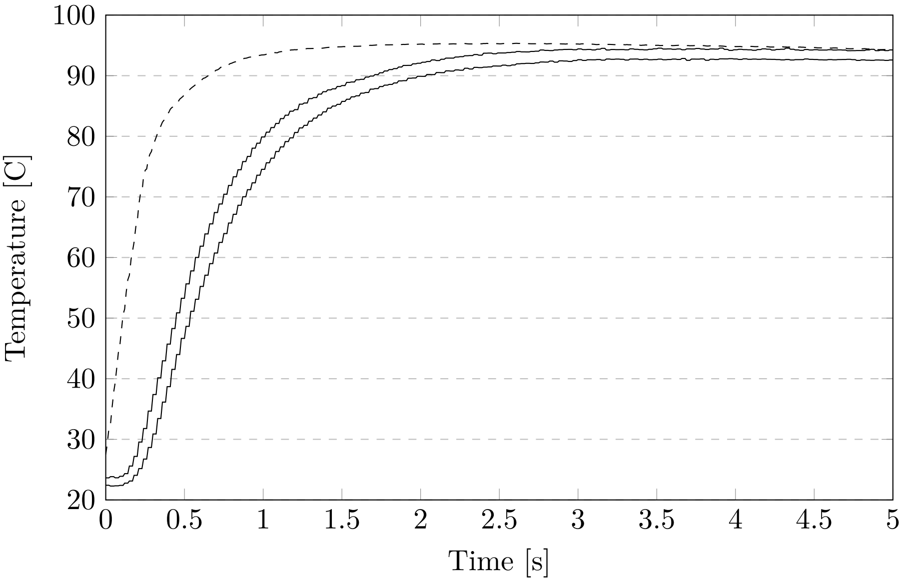

Figure 4.8: Solid lines - spread of temperature of the bottom at point P1; dashed line - averaged temperature of water at point P3

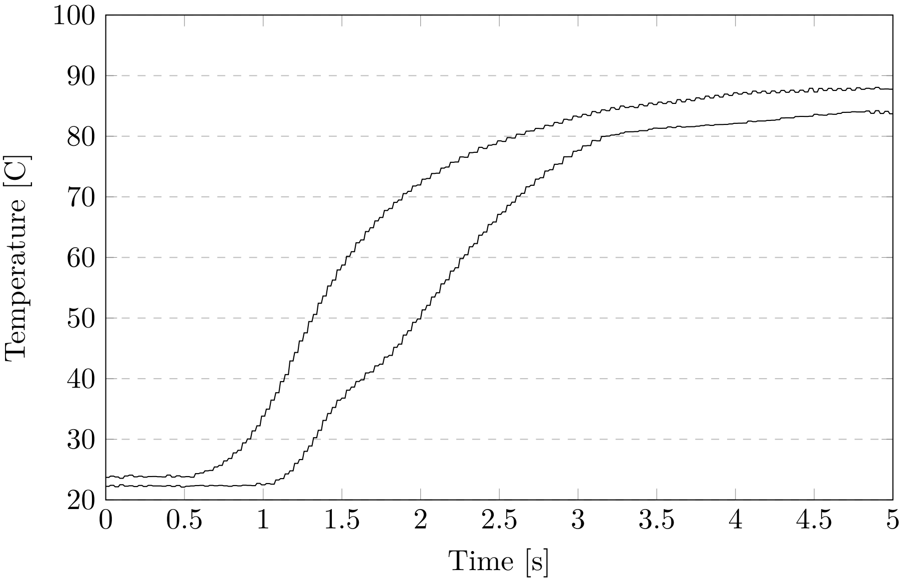

Figure 4.9: Spread of temperature of the bottom at point P2

displacement was in the range from -3.60 mm to -3.24 mm, relative to the initial position. The buckling jump occurred in the time range between 2.76 s and 3.70 s. The apparent stepped form of the graphs is due to the resolution of the high-speed camera and the absence of capture of the marker displacements below 1 pixel, that is 0.12 mm. Taking into account the accuracy of the displacement measurement of +/- 0.06 mm, the total spread of experimental results is shown in Fig. 4.11. It is worth noting here that no significant correlation was observed between the deformation records and the steel temperature records as well as the observed ambient temperatures. This means that the flow of water spilling over the bottom of the container, proceeding largely at random, had a significant impact here.

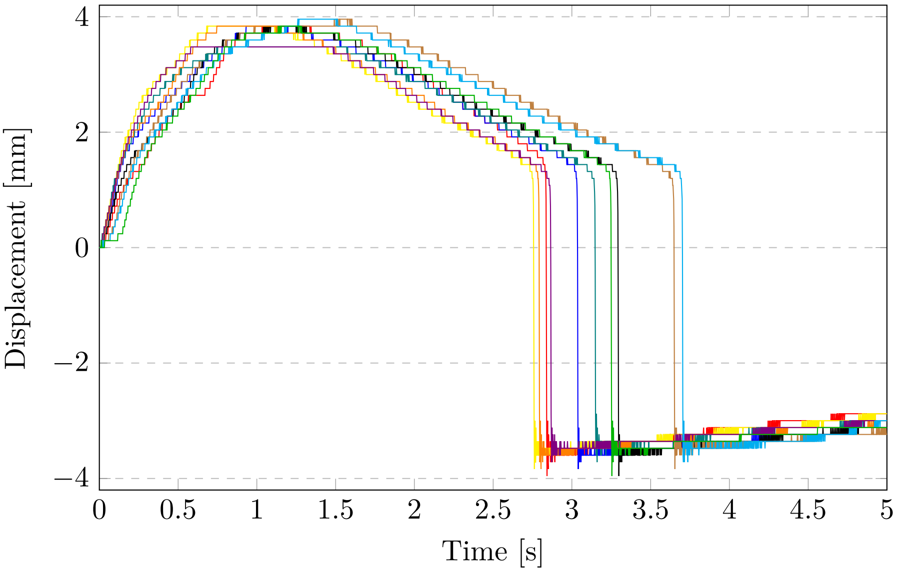

Figure 4.10: Vertical displacement of the bottom at point P1

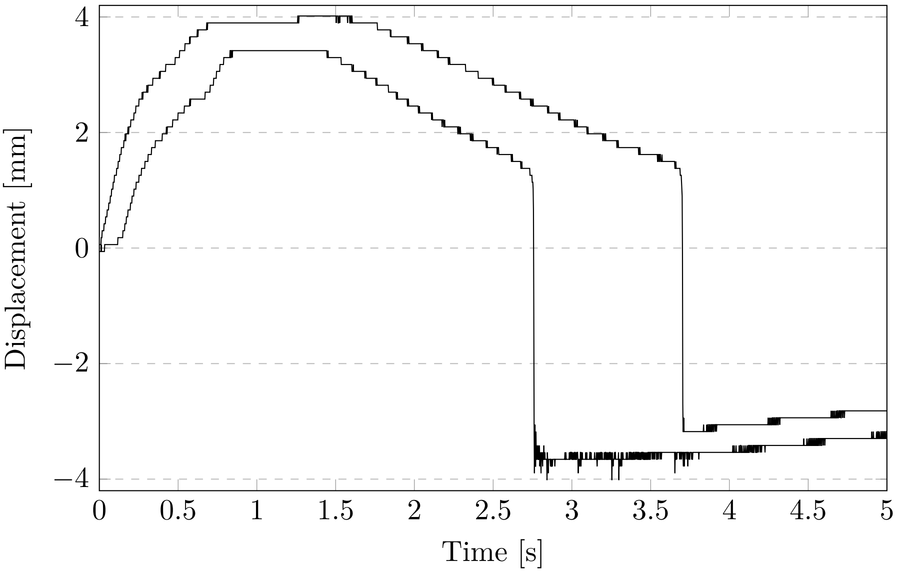

Figure 4.11: Spread of vertical displacement at point P1

Chapter 5

Coupled Thermal-FSI numerical analysis

5.1 Geometry and discretization of domains

Based on Fig. 4.1, for the coupled thermal-FSI numerical analysis, the geometry of the container was modeled as a symmetrical quadrant as shown in Fig. 5.1. The model contains a solid domain and a fluid domain excluding the geometry of the water feed tube. The planes of symmetry can be distinguished in relation to the shorter and longer edge of the quadrant of the container.

In order to carry out the analysis, 3D discretisation of both the solid and fluid domains was required. Here, it was decided to use a structured octagonal mesh - while its application using manual block methods is labour-intensive, it allows for faster numerical calculations and more reliable distributions of physical quantities. Keeping the two domains structured also allows their nodes to be fully mapped at the fluid-solid interface. Trial analyses have shown that for a solid body, taking the form of a 0.7 mm thick steel shell, two layers of 20-node finite elements are completely sufficient. Further increase in the number of elements by steel thickness did not alter the deformation pattern during the thermal test loads.

The structural discretisation of the fluid domain proved to be much more challenging. On the one hand, the high finite volume grid density of the relevant areas, i.e. the boundary layers and the water splash area in which droplet separation occurs, had to be maintained. On the other hand, it was important to keep reasonable computational costs, which increased very rapidly with each densification of the fluid domain. The area where the number of finite volumes could be reduced was the area of slow air movement, pushed out by the water.

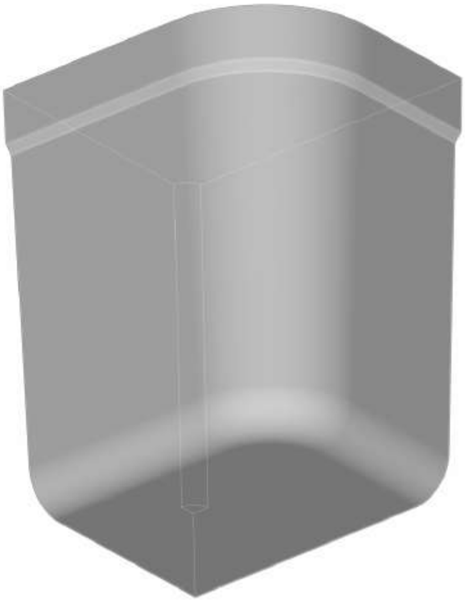

Figure 5.1: Geometry of the container for numerical analysis

5.1.1 Fluid domain mesh density analysis

A series of simplified non-stationary numerical analyses were carried out to determine the effect of the fluid domain mesh density on the representation of physical phenomena. Firstly, a 2D model was made based on the shorter-side symmetry plane of the container. It was estimated that water at 95.0°C flows out of the feed tube at a velocity of 1.9 m/s, pushing out air with an initial temperature of 23.1°C. For simplicity, the 2D axis of symmetry was assumed to be in the axis of water inflow. An adaptive method was applied for the size of the time steps, with a fixed Courant number of 0.5. The mesh research was performed for its 4 densities with the parameters shown in Table 5.1. An example of a structured 2D mesh of a simplified model created using the block method is shown in Fig. 5.2a.

The measured values were the time-varying phase fraction of water and the temperature at the assigned test point Pt (domain coordinates 105 mm x 5 mm). These parameters were intended to describe how the water front reaches the side of the tank, which is significantly influenced by the grid layout. This can take place in various ways, such as through drops overtaking the inflow front, as shown in Fig. 5.2b. Analyses conducted for different mesh densities showed some randomness in the spread of water. As shown in Fig. 5.3, the moment of the water front arriving at the Pt point differed between the extreme cases by 0.0014 s and had different patterns. However, there was no correlation with the increase in grid density. Similar results are given by the temperature curves at the Pt point, presented in Fig. 5.4. For this

Table 5.1: Parameters of analysed 2D mesh

Number of elements [$-$]	Max el. size [mm]	Min el. size [mm]
4.6k	3.5	0.05
8.9k	3.0	0.05
57.2k	1.0	0.05
259.2k	0.4	0.03

parameter, the spread of the contact moment was 0.0026 s. In conclusion, mesh density studies in this case do not clearly indicate the optimal number of elements. The differences in the densities showed time differences in fluid spread, but their values are lower than the spatial measurement error of the temperature sensor. In addition, given the rapid increase in required computing resources with each higher degree of grid density, no rationale was found for using denser variants.

Thus, it was decided to construct a structured 3D mesh based on the 2D "4.6k" variant. For the fluid domain, this resulted in a mesh of 588,508 hexagonal 8-node finite volumes, shown in Fig. 5.5a The height of the first element of the wall layer was maintained at 0.05 mm. Most of the elements achieved the quality above 0.95, with a minimum occurring value of 0.41.

5.1.2 Solid domain mesh

For the solid domain, two 20-node finite elements with a thickness of 0.35 mm were used for the cross section of the steel container wall. This gave 24,016 elements (Fig. 5.5b) with quality parameters overlapping with the fluid domain. For both domains, the maximum element dimension was 4.12 mm. A more detailed insight into the realization of the structural mesh connection, using the example of the splash area in the symmetry of the longer side, is shown in Fig. 5.6a. It can be observed here how local, horizontal densification of the fluid mesh affects the solid mesh (gray), while keeping the height of its elements constant. Meanwhile, Fig. 5.6b presents a characteristic section of the mesh resulting from the block approach, using the example of the bottom of the tank, under the water splash area.

5.2 Materials data

The numerical analysis distinguished between 4 materials: stainless steel AISI 201 and High Density Polyethylene (HDPE) for the solid domain and, along with water and air for the fluid domain. Material data were linearly interpolated for different temperatures. As the temperatures in the experiment ranged from 23.1 to 95.0°C, the range for the materials

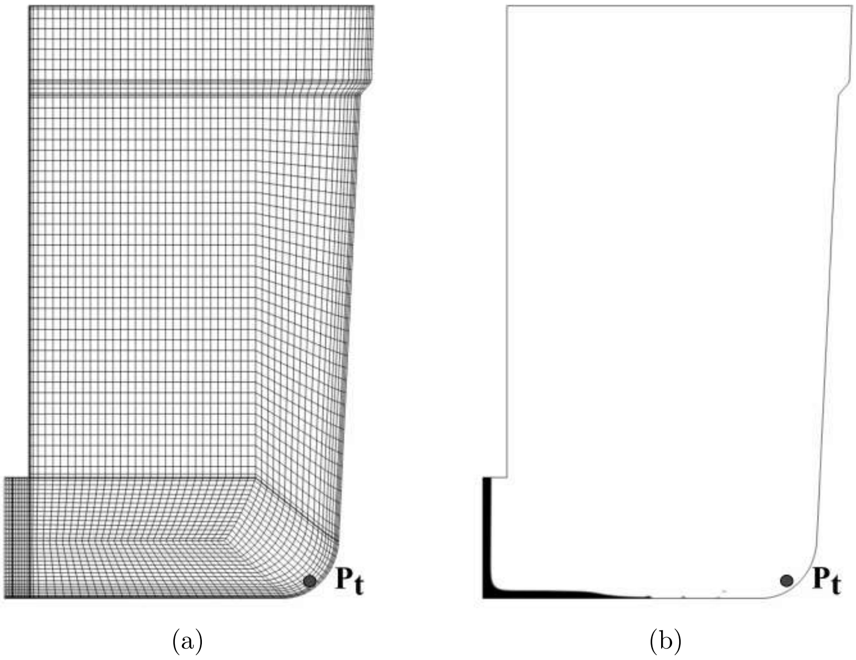

Figure 5.2: Sample 2D mesh with 4.6k elements (a) and example of droplet splitting (b)

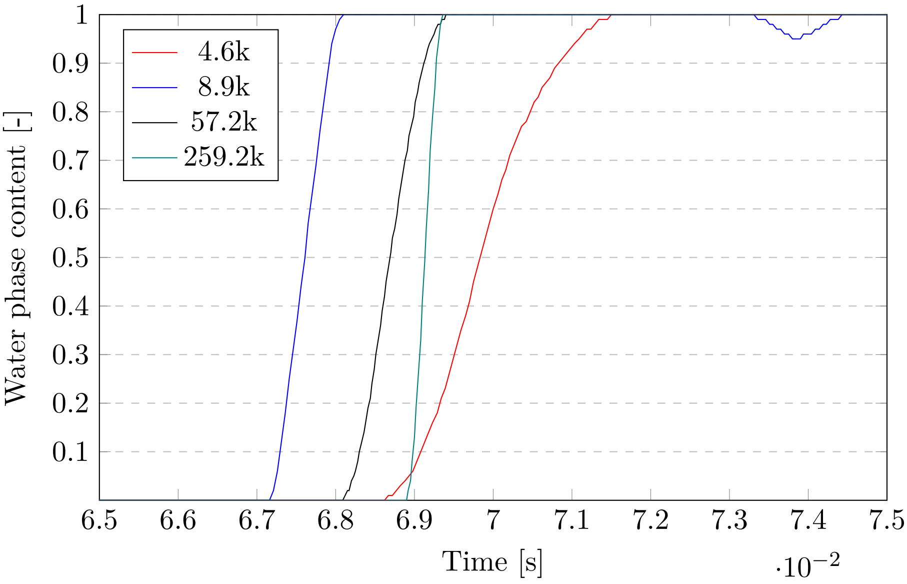

Figure 5.3: Water phase content at point Px for different mesh densities

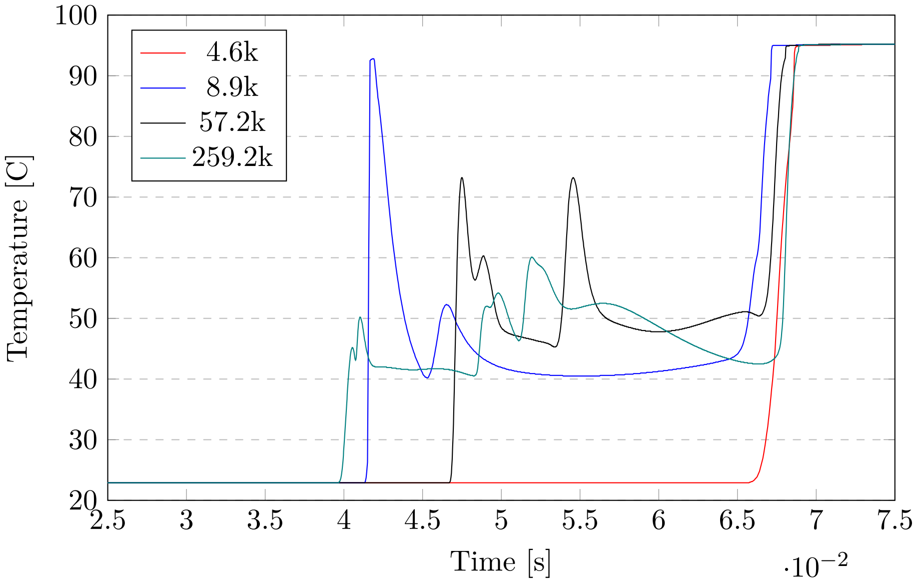

Figure 5.4: Temperature at point Px for different mesh densities

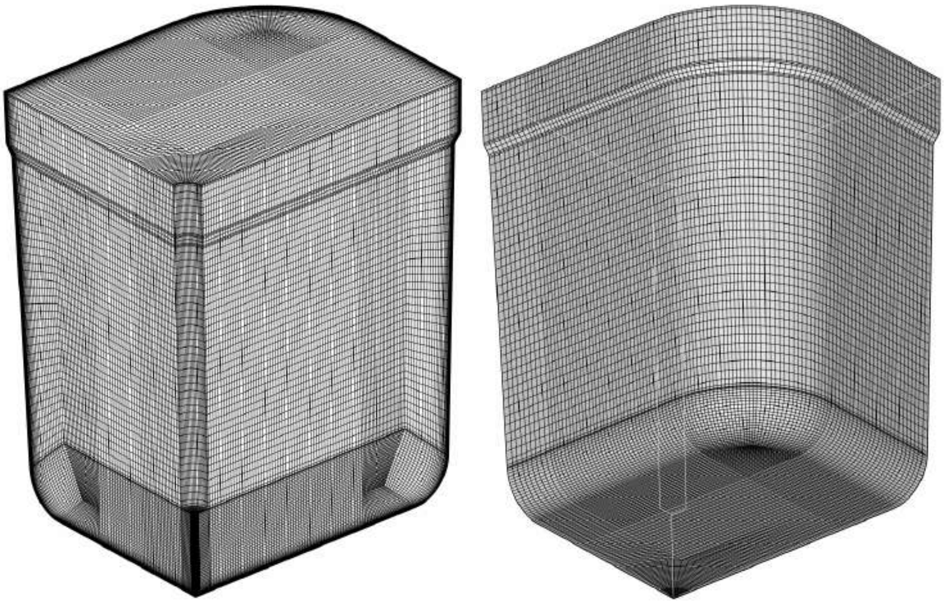
(a)
(b)

Figure 5.5: Mesh of fluid (a) and solid (b) domain used in numerical analysis

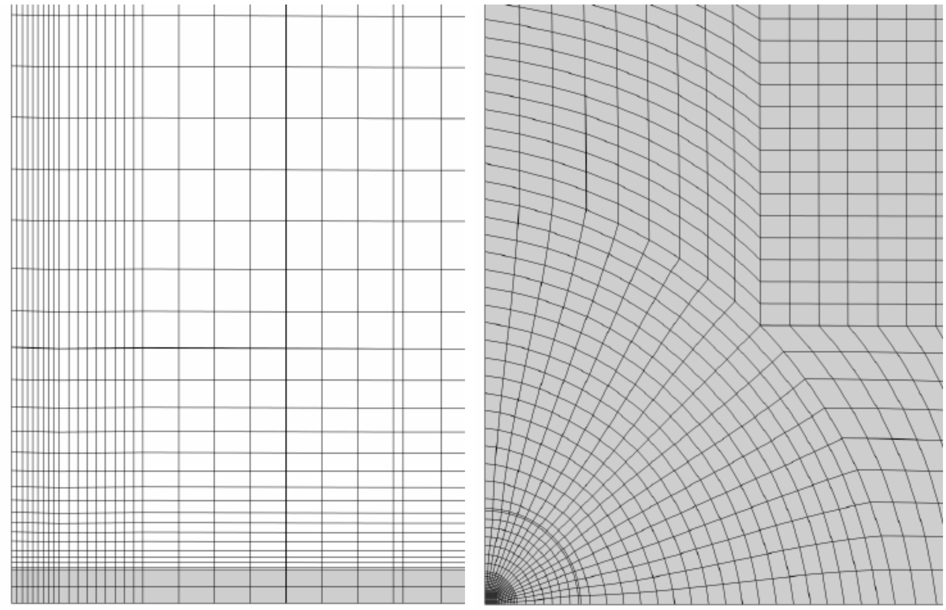
(a) (b)

Figure 5.6: Side view of the water splash area with boundary layer (a) and bottom view of the container (b)

in the numerical analysis was extended to 20-99°C. The adopted material data for stainless steel at selected temperatures are shown in Table 5.2. Here the temperature-dependent coefficient of thermal expansion α, thermal conductivity coefficient of solid β_S and Young's modulus are presented. Meanwhile, a constant density of 7800 kg/m3 was assumed, as well as a constant Poison's coefficient of 0.27 and specific heat of 501.6 J/(kg K). HDPE occurs here as the material of the water supply tube. Since it is a minor object, fixed values were assumed for it: ρ = 940.0 kg/m3, C_p = 2.25 kJ/(kg C), β_S = 0.44 W/(m °C). Then, the adopted properties in relation to temperature for air are presented in Table 5.3, and for water in Table 5.4. In this case, the parameters distinguished are : density ρ, specific heat Cp, thermal conductivity coefficient of fluid β_F and viscosity μ. For water, the surface tension coefficient σ is additionally listed.

Table 5.2: Material properties of stainless steel AISI 201

T $[°C]$	α $[1/°C]$	β_S $[W/(m°C)]$	Young's Modulus $[MPa]$
20	1.58e-05	15.26	2.00e+05
60	1.60e-05	15.79	1.97e+05
99	1.62e-05	16.25	1.94e+05

Table 5.3: Physical properties of air

T $[°C]$	ρ $[kg/m^3]$	Cp $[kJ/(kg°C)]$	β_F $[W/(m°C)]$	μ $[kg/(ms)]$
20	1.20	1.006	0.0257	1.827e-05
60	1.07	1.008	0.0288	1.958e-05
99	0.95	1.011	0.0316	2.114e-05

Table 5.4: Physical properties of water

T $[°C]$	ρ $[kg/m^3]$	Cp $[kJ/(kg°C)]$	β_F $[W/(m°C)]$	μ $[kg/(ms)]$	σ $[N/m]$
20	998.19	4.18	0.598	1.00e-3	0.073
60	983.19	4.19	0.651	4.67e-4	0.066
99	959.09	4.21	0.677	2.82e-4	0.060

5.3 Solvers settings and boundary conditions

5.3.1 System Coupling solver

The System Coupling software within the ANSYS Workbench 20.2 package was used to couple the CFD and CSD solvers. Thus, two participants were defined here: Fluent and Transient Structural, as the Mechanical module. Data transfer was carried out through the FSI interface, which was the inner wall of the container. From the Fluent side, force, heat transfer coefficient and near wall temperature were transmitted. Transient Structural, on the other hand, sent temperature and displacement. The System Coupling analysis requires one common time step for both solvers, which in this case was set to 0.0001 s. The minimum number of coupling iterations in each time step was set to 1 and the maximum to 5.

5.3.2 Computational Fluid Dynamics solver

As a Computational Fluid Dynamics solver, ANSYS Fluent 20.2 software was used. The homogeneous volume of fluid multiphase model was applied here. Air was specified as the primary phase, and water as the secondary phase. Volume fraction formulation was set to explicit with the Courant number of 0.25. In contrast, implicit formulation was used for body force. For interface modeling, the sharp type was used with a hybrid sub-time step calculation method. On the purpose of surface tension modeling, the continuum surface stress model was chosen along with the piecewise-linear surface tension coefficient, the values of which were given in Table 5.4. Fluid flows during the numerical analysis presented a significant degree of variation.

While water flowing out of the tube had a laminar nature, there occurred local increases in Raynolds number and formation of vortices on the bottom during the water spreading. Similarly, the air, which was pushed out relatively slowly by the water, formed intense vortices near the hot water inlet. In order to comprehensively cover the phenomena occurring in the entire fluid domain and to obtain stability in the calculations, a 2-equation k-omega SST viscous model with a production limiter option was used, including solver default values for the model constants.

In general, Pressure-Velocity Coupling was performed using the Coupled Scheme along with First Order Implicit transient formulation. Within the spatial discretisation, the Second Order Upwind method was used for the momentum, turbulent kinetic energy, specific dissipation rate and energy equations. In turn, the gradient was calculated using the Least Squares Cell-Based method and the volume fraction with the Geo-Reconstruct algorithm. The Body Force Weighted method was used for pressure calculations due to the significant impact of density differences.

For this work, two non-stationary VOF analyses were performed: FSI and CHT. In the first case, within the System Coupling, the displacement and temperature from the CSD solver was transmitted to the no slip fluid wall - the solid domain interior was not present in the CFD solver. A Dynamic Mesh model with Implicit Update and Diffusion Smoothing options was used to model the moving container wall on the Fluent side. The second option used the Boundary Distance Function with the Diffusion Parameter equal to 1.2. Within Dynamic Mesh Zones, the Cell Height parameter of 0.002 m was assumed on fluid wall, and a deforming type was established on the fluid interior and symmetries. For the CHT analysis, grid movement was not taken into account. As both the fluid and solid domains were fully present, all heat transfer was calculated within the Fluent solver. For this, it was necessary to assume properties resulting from ambient convection of air on the outer wall of the container - Heat Transfer Coefficient of 15 W/(m^2 °C) and a Free Stream Temperature of 23.1°C.

The inlet boundary condition for both cases was defined as velocity-inlet at a gravitational acceleration of 9.81 m/s^2 with a volume fraction of the water phase equal to 1. Here, a constant fluid velocity in the vertical direction estimated from experimental measurements of 1.89 m/s was assigned. As the actual inlet temperature was variable, while having a significant influence on thermal phenomena, the temperature was set as a time-varying characteristic based on averaged measurements at point P3, according to Figure 4.8. The presence of the HDPE water supply pipe was modelled as its outline in the form of a no-slip wall. The outlet of the pushed out air was defined in the upper plane of the fluid domain. An atmospheric pressure condition was set along with an ambient temperature of 23.1°C. The location of the boundary conditions in the fluid domain is shown in Fig. 5.7. The time step for the flow analyses was 0.0001 s, resulting in the Courant number between 0.6

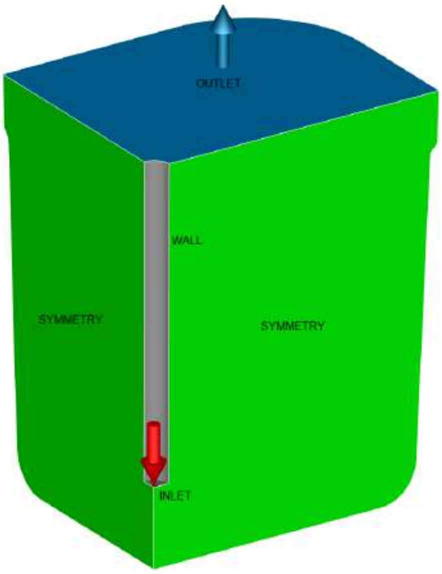

Figure 5.7: Boundary conditions for the CFD solver

and 1.0. Flow data were recorded with an interval of 0.005 s. In the case of Thermal FSI analysis, a full record of the deformed mesh was also required at each data save point.

5.3.3 Computational Solid Dynamics solver

The FEM mesh of the container quadrant was loaded into the Transient Structural module of ANSYS Mechanical 20.2. Two Mechanical APDL scripts were required here: the first converted Type 186 elements to Type 226 elements, and the second initialised the ambient temperature 23.1°C in the new elements. Standard earth gravity was assumed and the fixed support boundary condition was located at along its upper edge as an Fig. 5.8. Also, symmetry conditions were applied along both side edges of the quadrant. In the case of the Thermal FSI analysis, the entire inner wall of the container served as the FSI interface, providing force, heat transfer coefficient and near wall fluid temperature. However, a comparative heat transfer analysis was also carried out, where a temperature field was applied to the bottom of the tank, varying according to the graph in Fig. 4.8. This boundary condition corresponded to the water contact area, covering in addition to the bottom plane also the side walls to a height of 1.25 mm. Within the nonlinear controls of the Mechanical solver, the Program Controlled option was adopted for force, momentum, displacement, rotation and linear search convergence. In

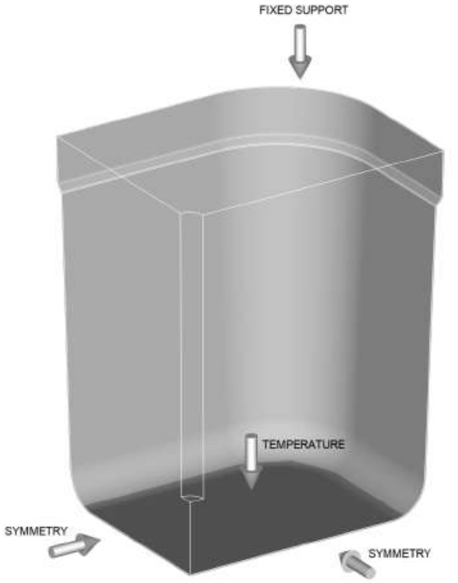

Figure 5.8: Boundary conditions for the CSD solver

contrast, the Full option was selected for the Newton-Raphson method.

5.4 Results

For the purpose of comparing different types of simulation with experimental results, 3 analyses were carried out: Thermal FSI, Fluent CHT and Thermal Mechanical. The role of the Thermal Fluid-Structure Interaction numerical analysis, being the most complex, was to capture as many of the relevant physical phenomena that occurred within the experiment as possible. Referring to Fig. 4.5, by observing the water phase, here also three characteristic moments could be captured, as shown in Fig. 5.9, where the view of the multiplied quadrants of the container was used. Firstly, the water started to form a vortex ring as soon as it hit the bottom of the container (5.9b). Then, the water spread relatively more slowly across the bottom until it reached the sides (5.9c). Finally, the phase of slow filling of the container was interrupted by buckling of its bottom, breaking the water film (5.9d). In addition, figure 5.10 shows half of the central section along the longer side. It can be seen here how the shape of the bottom influences the behaviour of the fluid, noting its highest position 5.10b and lowest position 5.10d. It is worth pointing out that no ejection of water phase droplets was observed, as in the case of the experimental tests. Relatively low level of coverage in time of the experimental phenomena with the results of the numerical analysis can also be seen. One of the most important results here, however, is the timing of the bottom jump, which occurred at the latest at 3.70 s for the

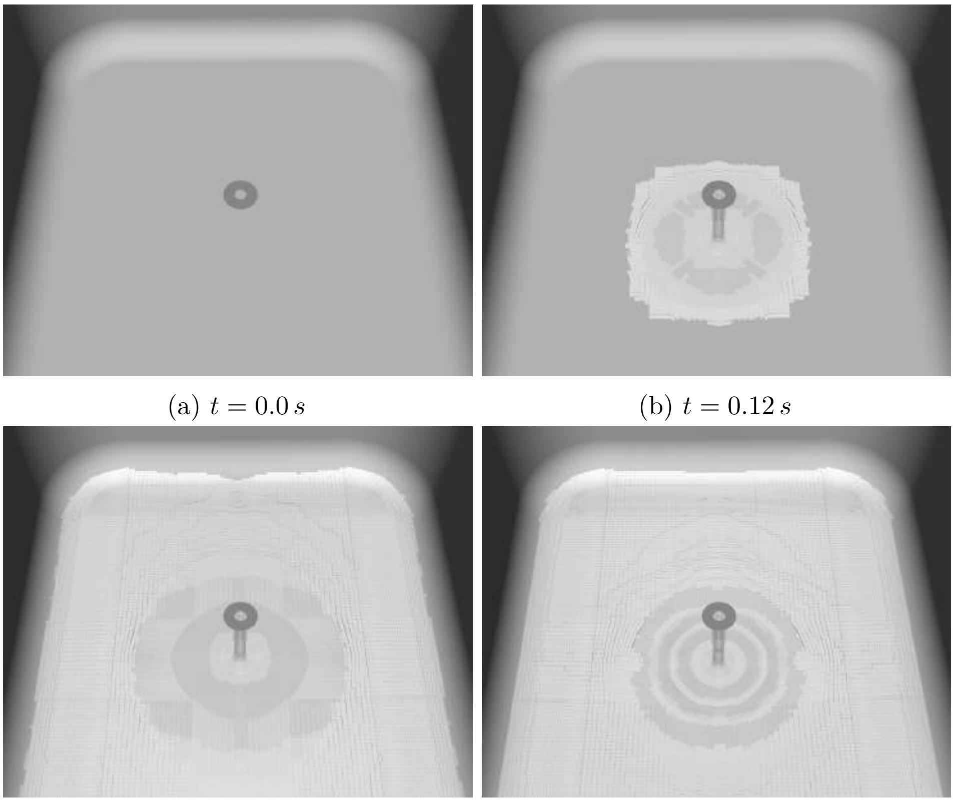

(a) $t = 0.0\,s$ (b) $t = 0.12\,s$

(c) $t = 3.20\,s$ (d) $t = 4.13\,s$

Figure 5.9: Water distribution in the container during numerical analysis

experiment and at 4.11 s for the analysis, resulting in a 0.39 s difference.

The water phase spreading across the bottom of the container was subjected to cooling from both steel and air. As shown in Fig. 5.11a, using the t = 0.12 s example, the liquid here moves faster than the temperature of the solid. In contrast, Fig. 5.11b shows not only the cooling of the liquid, but the dissipation of heat into the air and steel.

The next example, shown in Fig.5.12, shows a comparison of the the temperature distribution of the steel on the tank top surface at times t = 0.12 s and t = 3.20 s. It can be seen here that the instantaneous maximum simulation temperature of 52°C in the initial phase does not occur at all, despite the contact between the liquid with the solid. When the entire bottom of the tank is covered with water, the maximum temperature is practically halfway to the side wall. A comparison of the temperature at point P1 from the Thermal-FSI, Thermal Mechanical and Fluent CHT analyses with the experimental results is shown in Fig. 5.13. It can be seen here that the numerical results were not contained within the area of the experimental results, being however in relative proximity. At the

(a) $t = 0.12\,s$

(b) $t = 3.20\,s$

(c) $t = 4.11\,s$

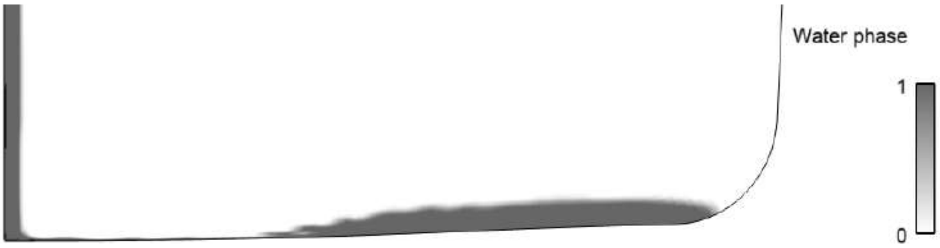

(d) $t = 4.13\,s$

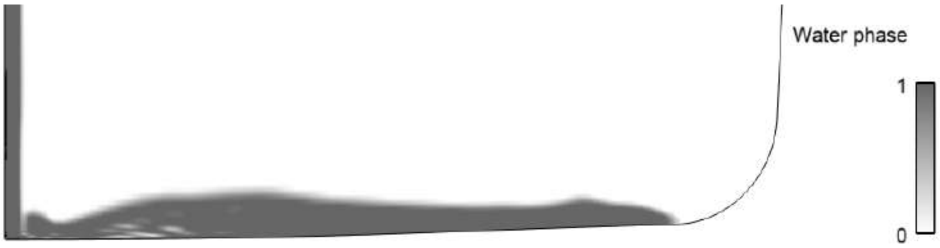

(e) $t = 4.50\,s$

Figure 5.10: Water distribution and the shape of the container bottom during numerical analysis - symmetry plane along the longer side

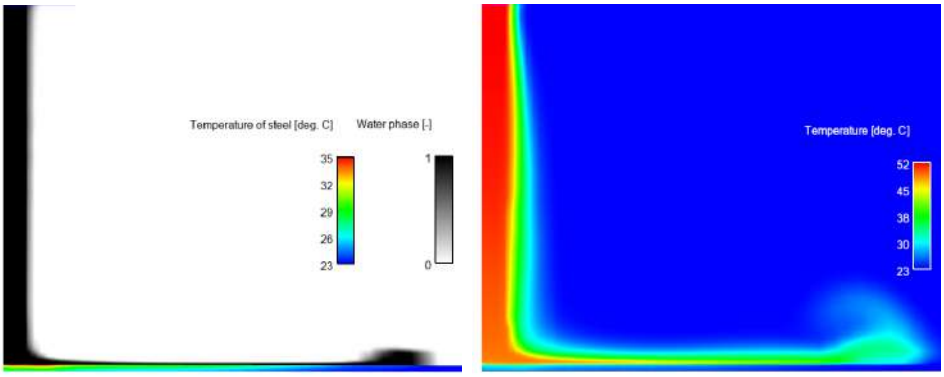

(a) (b)

Figure 5.11: Side view of water distribution and temperature at time $t = 0.12\,s$

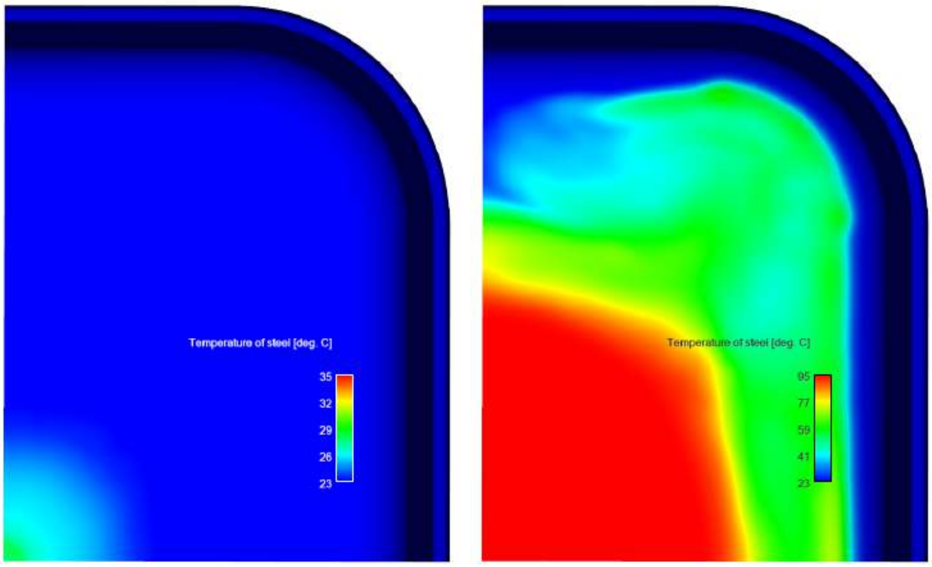

(a) $t = 0.12\,s$ (b) $t = 3.2\,s$

Figure 5.12: Steel temperature - top view

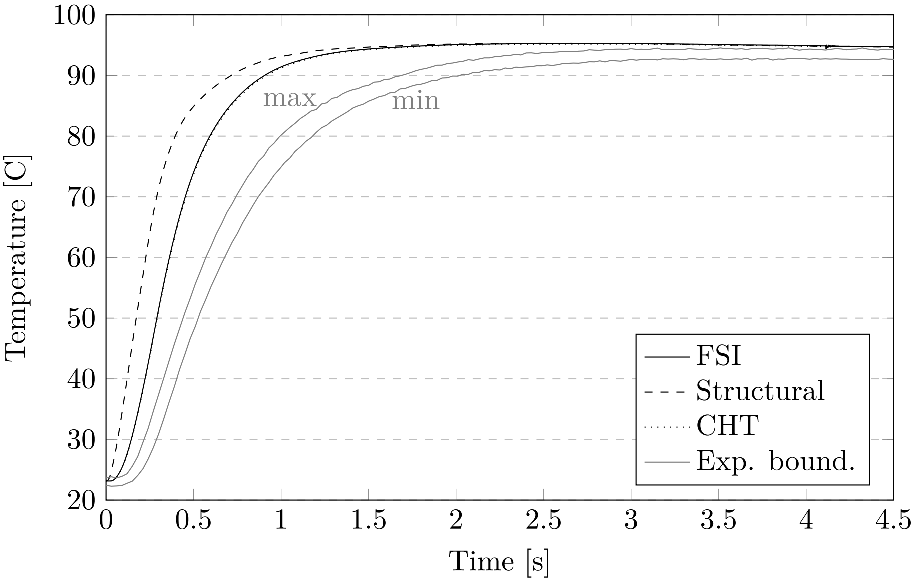

Figure 5.13: Temperature of steel at point P1 - numerical analysis and experiment

central point of the container, and thus the central point of water impact, the temperature curves from the flow analyses overlap, being closer to the experimental curve than the Thermal Mechanical analysis. In this case, the maximum discrepancies between the results of the numerical analyses and the area of experimental results were, respectively: for the Thermal Mechanical analysis 36.4°C at 0.35 s, for the Fluent CHT analysis 21.2°C at 0.48 s, and for the Thermal FSI analysis also 21.2°C at 0.48 s.

Next, Fig. 5.14 shows the temperature curves of the three analyses and the experiment at point P2. Here, the maximum differences from the boundaries of the experimental results were: 70.9°C at 1.07 s for Thermal Mechanical analysis, 26.6°C at 3.15 s for the Fluent CHT analysis, and 21.2°C at 2.37 s for the Thermal FSI analysis. Moving forward, a comparison was made between the non-stationary displacements in point P1 obtained in the numerical analyses and the displacement from the experiment. Its results are shown in Fig. 5.15. In this case, the Thermal Structural analysis showed a large divergence from the experimental results area, reaching a maximum of 5.82 mm in 1.17 s, corresponding also to a maximum deformation of 2.40 mm - with the opposite direction to the direction in the experiment. It is worth noting here that the non-linear behaviour of the tank geometry was not captured.

This, in turn, has been achieved in the Thermal-FSI analysis. The rapid buckling of the bottom of the container occurred at 4.11 s, that is 0.39 s after the buckling range in the experiment. The maximum difference between

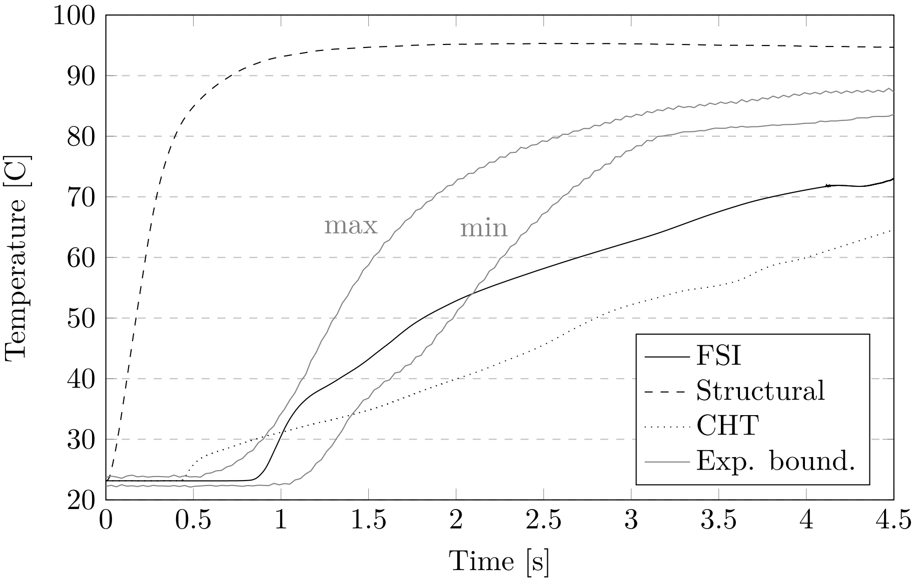

Figure 5.14: Temperature of steel at point P2 - numerical analysis and experiment

numerical and experimental displacement can be indicated as 5.20 mm at 3.70 s. However, excluding from the results the moment of the jump of the tank bottom, the largest deviation from the experimental results area was 1.01 mm, rounded at the same time point. In addition, the maximum displacement value for the Thermal-FSI analysis was within the maximum experimental values, reaching 3.52 mm at 1.29 s. Due to the presence of the CSD solver in both the Thermal Structural and Thermal FSI analyses, it is possible to determine not only deformations but also stresses - which were not experimentally verifiable in this study. Fig. 5.16 shows the areas where the highest Huber-Mises-Hencky reduced stresses occurred. For the Thermal Structural analysis, the maximum reduced stress was 173 MPa at 0.86 s and was located on the outside corner of the container. For the Thermal FSI analysis, in contrast, the maximum reduced stress was 176 MPa and occurred at 3.20 s on the inner side of the longer wall bend. The curves of the maximum occurring HMH reduced stress for the entire geometry during the simulations are shown in Fig. 5.17. It can be seen here that while the maxima have similar values, locally the Thermal FSI analysis shows higher stresses for most of the analysis time. Looking at the stresses in more detail, the outside midpoint P1 was taken as an example and the normal stresses in the two directions parallel to the bottom plane were determined there, as the perpendicular stresses reached negligible values. Normal stresses with a direction along the long side have been denoted as σ_{xx} and along the short side as σ_{yy}, taking their positive values as tension and their negative values

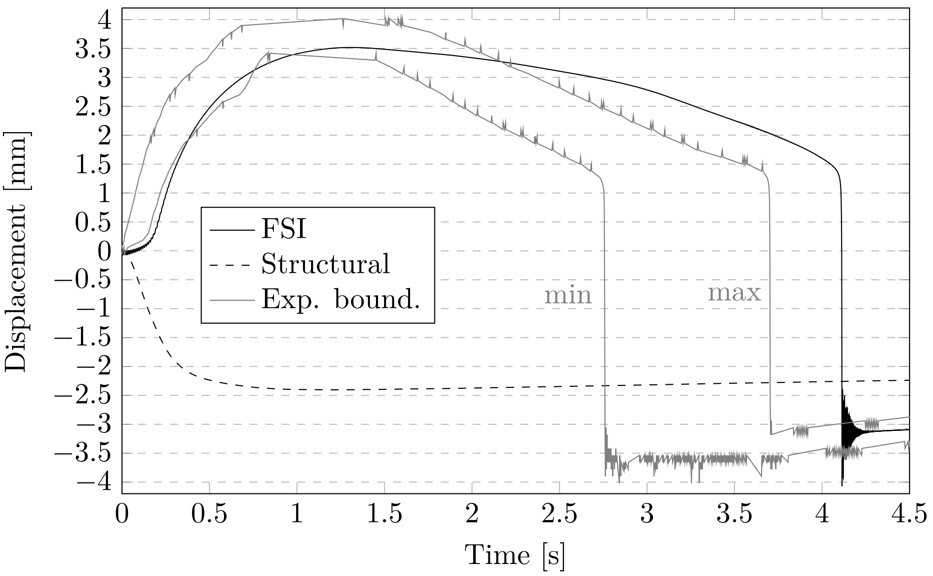

Figure 5.15: Vertical displacement of steel at point P1 - numerical analysis and experiment

as compression. The normal stress curves shown in Fig. 5.18 show significant variation in both the values and type of stresses. Thermal Structural analysis showed the highest tensile stress of 40 MPa at P1 at 0.22 s. Meanwhile, the Thermal FSI analysis, showing compressive stresses prior to buckling, determined the maximum stress value to be 147 MPa during buckling with its change to tensile stresses.

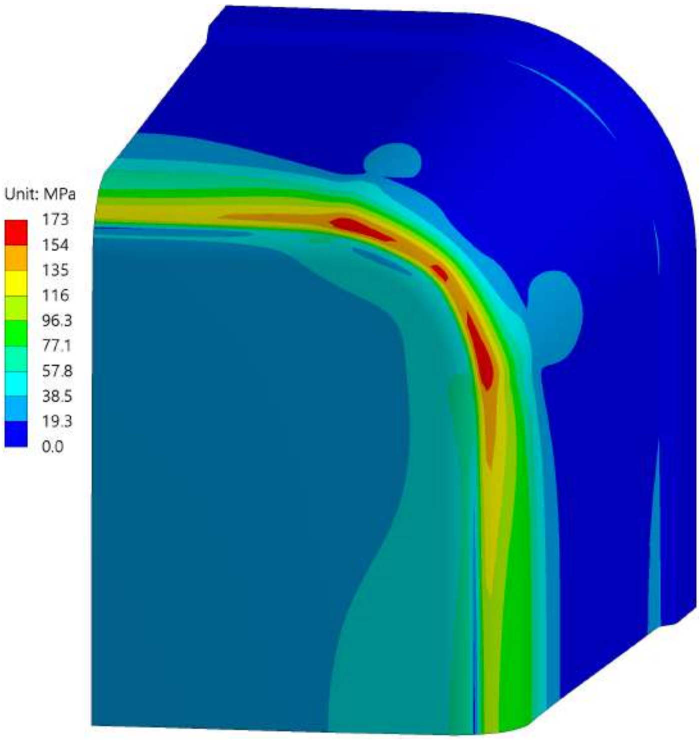

(a) APDL, $t = 0.86\,s$

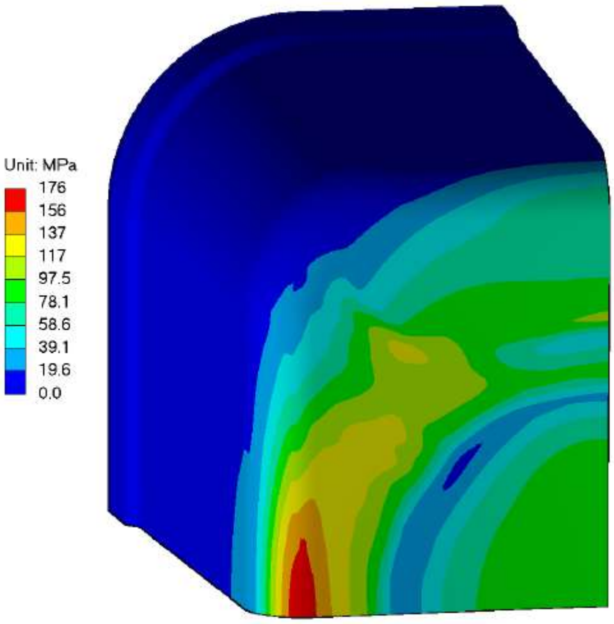

(b) FSI, $t = 3.20\,s$

Figure 5.16: Maximum HMH stress in thermal structural analysis, bottom view (a) and FSI analysis, top view (b)

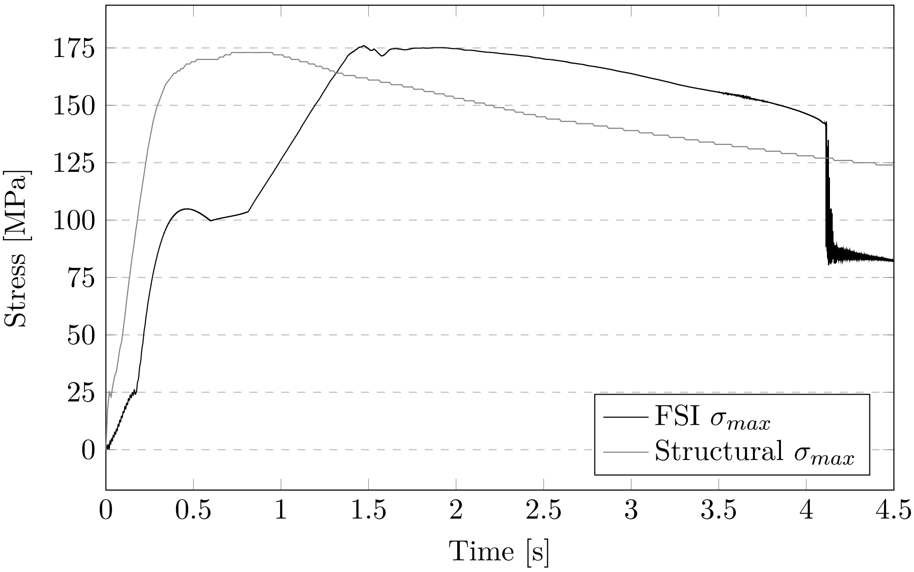

Figure 5.17: Maximum HMH stress in steel - FSI analysis and thermal structural analysis

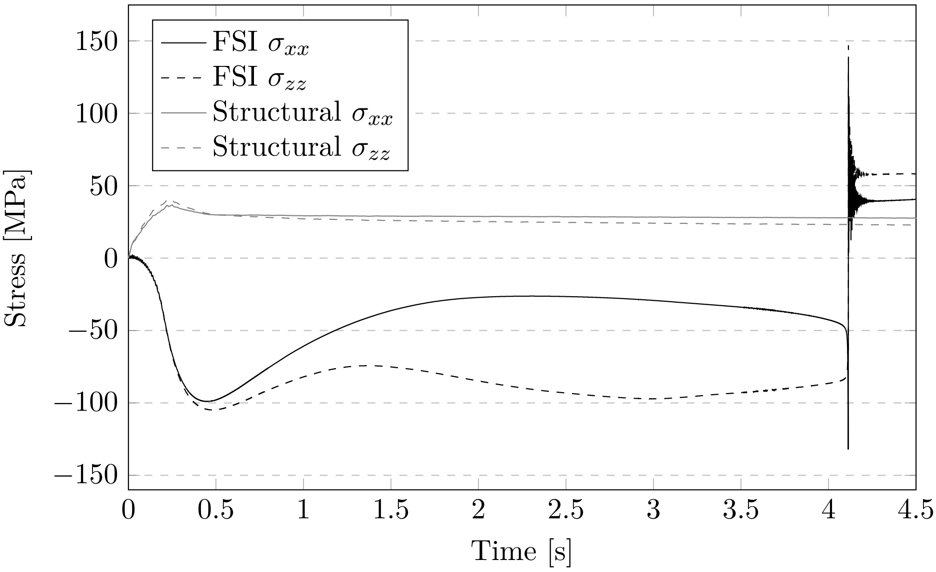

Figure 5.18: Normal stress σ_{xx} and σ_{zz} in steel at point P1 - FSI analysis and thermal structural analysis

Chapter 6

Conclusions

This thesis examined the relevance of a computational method such as Thermal Fluid - Solid Interaction analysis in the context of rapid thermal loads. The inspiration to address this topic came from the power engineering industry. The increasing share of renewable energy sources in the grid structure is resulting in the need for ever faster start-ups and shutdowns of thermal power machinery. Going into the details of these processes and taking the cooling systems of steam turbine blades and casings as an example, a picture emerges of alternately heated and cooled steel structures. Thus, the need to predict the thermal expansion and stress behaviour of these structures arises.

However, reducing the time scale of the thermal loads in question from hours and tens of minutes to seconds, the likelihood of non-linear effects increases. This, in turn, increases the significance as well as the area of application of the Thermal FSI numerical analysis. For the power engineering industry, it could be gas turbine start-up simulation. Following this line of thought, even more challenging may be load changes for aircraft turbines, where the weight of the materials used is crucial. The issue does not only apply to rotating machinery - it is certainly worth considering jet engines here, where the rapidity of thermal loads is much greater. The same applies to rocket engines, with applications both in the military and in the thriving space transport industry.

Considering the above mentioned potential applications, and with respect to the literature review, the topic of Coupled Thermal FSI numerical analyses appears to be significantly undeveloped. This seems quite surprising given the high level of general insight into the Conjugated Heat Transfer and Momentum FSI methods. Particularly notable is the shortage of experiments verifying Thermal FSI approach, and thus shortage of reproducible benchmark analyses.

For this very reason, this dissertation aims to provide initial direction for research on the verification of the Coupled Thermal FSI method. The focus here was on demonstrating the ability to capture non-linear phenomena that are not present in decoupled numerical analyses. A search was carried out for a structure that exhibits non-linear behaviour when in contact with a hot fluid every time. For this purpose, an open stainless steel thin-walled container was selected and thermally loaded with hot water.

A test stand was then constructed, based on the selected object. Four measurement points were included:

- measurement of the temperature of the steel in the centre of the tank bottom, on the outer side,
- measurement the temperature of the steel, 80 mm along the shorter edge from the centre, on the outer side,
- measurment of the temperature of the water leaving the feed tube,
- measurement of the displacement of the steel, in the centre of the tank bottom.

Measurements were taken continuously for 5 seconds for each of the 10 hot water doses, preceded by drying the tank. In this way, taking into account the measurement uncertainties of the apparatus used, a range of time-varying values was determined for comparison purposes for numerical analysis. Buckling of the bottom of the tank was noted with each experimental trial. The formation of a vortex ring and the ejection of droplets during buckling could be regarded as repeatable, characteristic features in the water flow. Besides, the water distribution showed a certain randomness. The average temperature of the water leaving the tube was 95°C, with an estimated average velocity of 1.9 m/s and an ambient temperature of 23.1°C. Due to thermal deformation, the bottom of the tank first deformed upwards by a maximum of 3.96 mm and then jumped downwards to a position a maximum of 3.60 mm lower than the initial position. The jumps occurred between 2.76 s and 3.70 s of the experiment time.

With an experimental base, it was possible to move on to verify the Thermal-FSI approach. The software that made this possible was the ANSYS package version 20.2. Fluent was used as the CFD solver and the Mechanical module as the CSD solver. The two solvers were combined by a third one, called System Coupling. The model was simplified to a quarter of a container with two planes of symmetry. The Volume of Fluid method had to be used on the fluid side to represent the ejection of the air present in the tank by the inflowing water. The Dynamic Mesh method was responsible for the displacements in the fluid domain. In the solid domain, on the other hand, a conversion of the mesh element type was required, to support both heat transfer and deformation. A grid density selection was then performed which, while for the solid domain was not demanding, there was a need for a deeper analysis for the fluid domain. A 2D mesh analysis was then performed for

Table 6.1: Summary of highest deviations in results of numerical analyses in relation to the experimental boundaries

Analysis type	Maximum deviation P1 temp. [°C]	P2 temp. [°C]	P1 displ. [mm]	Buckling time [s]
Coupled Thermal-FSI	+21.2	-21.2	+5.20/1.01	-0.39
CHT	+21.2	-26.6	-	-
Thermal Structural	+36.4	+70.9	-5.82	-

non-stationary water spreading, which, however, did not give conclusive results. A variant with a lower number of elements was therefore chosen, leaning towards a lower computational load. In this way, a structural mesh was finally obtained with 24,016 finite elements for the solid domain and 588,508 finite volumes for the fluid domain.

Finally, the Copled Thermal-FSI analysis was carried out, as well as comparative, transient Conjugated Heat Transfer and Thermal Structural analyses. In general, the results of the numerical analyses here are characterised by a certain discrepancy with the experimental results. The value curves of the calculated parameters at the measurement points are mostly not in the area of the experimental curves. This is due to certain intentional simplifications relative to actual conditions, i.e. constant thickness of the steel tank bottom or constant discharge velocity from the water dosing tube. However, this does not hinder the representation of the main theme of this dissertation, i.e. the peculiarities and advantages of Thermal-FSI analysis over other, adequate types of analysis. A summary of the maximum deviations from the experimental curves of the three analyses performed is shown in Table 6.1.

Altogether, the application of the Coupled Thermal-FSI analysis in the case under consideration has led to the following observations:

- Coupled Thermal-FSI analysis obtained the curves of the variables closest to the experimental curves.
- Coupled Thermal-FSI analysis properly captured most of flow phenomena, i.e. vortex formation or rupture of the liquid film.
- Due to the consideration of fluid flow, Coupled Thermal-FSI analysis allows heat transfer to be very closely mapped in a solid body.
- Due to the consideration of thermal deformation, Coupled Thermal-FSI analysis allows the secondary effect of the solid on the flow to be mapped.
- In relation to transient Conjugated Heat Transfer and Thermal Structural

analyses, only Coupled Thermal-FSI analysis allowed the capture of the non-linear phenomenon of buckling of the steel container bottom.

- The Coupled Thermal-FSI analysis did not record the ejection of water droplets into the air when rapid buckling occurred, as it accured in the experiment.
- The Coupled Thermal-FSI analysis also allowed for a more accurate determination of stress variations. While the values of the maximum reduced stresses did not differ significantly from those obtained in the Thermal Structural analysis, their location was different. However, in the case of time-varying normal stresses, changes in stress type and an instantaneous maximum of 100 MPa higher were noted.
- The Coupled Thermal-FSI analysis had several times the calculation time of the CHT analysis and an order of magnitude more time than the Thermal Structural analysis.
- In the Coupled Thermal-FSI analysis, the time step has the same value for the CFD solver and the CSD solver. Due to the characteristics of the software used, the results of the CSD solver were saved with each time step, resulting in very large files that were problematic to process.

It is worth noting that during the experiment, the buckling of the tank was accompanied by a distinctive sound, thus the current analysis could successfully be extended to acoustic analysis. This is encouraged by the captured oscillatory bottom movements after the jump. However, this would require a more accurate mesh and more demanding solver settings.

What appears to be important here is the lack of water droplet ejection during buckling. This seems to be caused by the lack of momentum transfer from the solid to the fluid domain through the FSI interface. In other words, the CFD solver does not receive information about the mass of the solid. This is certainly an interesting aspect, the study of which can be used to further develop the Coupled Thermal-FSI method.

The above remarks give a picture of a numerical method that offers great analytical possibilities, but at a high computational cost. Therefore, its use is justified when non-linear behaviour is suspected in a given structure under thermomechanical study or other numerical methods fail to reproduce the desired behaviour.

Appendix A

Mechanical APDL script

```
! Pre-processing:
/PREP7

! Get maximum element type:
*get,etype_num,etyp,0,num,max

! Define Element types:
et,etype_num+1,solid226,11

! Change hex20 elements (type 186) to element
  ID type etype_num+1 (type 226):
esel,s,ename,,186
emodif,all,type,etype_num+1

! Activate all elements
esel,all

/SOLU

! Set initial temperature to 23.15 C:
IC,all,temp,23.15
```

List of Figures

List of Tables

Bibliography

[1] "Kyoto protocol to the united nations framework convention on climate change," *United Nations*, 1998.

[2] "Directive 2009/28/ec of the european parliment and of the council of 23 april 2009 on the promotion of the use of energy from renewable sources and amending and subsequently repealing directives 2001/77/ec and 2003/30/ec," *Official Journal of the European Union*, 2009.

[3] M. Banaszkiewicz, "The low-cycle fatigue life assessment method for online monitoring of steam turbine rotors," *International Journal of Fatigue*, vol. 113, pp. 311–323, 8 2018.

[4] M. Banaszkiewicz, "Steam turbines start-ups," *Transactions of the Institute of Fluid-Flow Machinery*, vol. 129, pp. 169–198, 2014.

[5] M. Bryk, M. Banaszkiewicz, T. Kowalczyk, W. Dudda, and P. Ziółkowski, "Slowly-closing valve behaviour during steam machine accelerated start-up," *Case Studies in Thermal Engineering*, vol. 39, 11 2022.

[6] "European aviation environmental report," *European Environment Agency, European Aviation Safety Agency, Eurocontrol*, p. 107, 2019.

[7] "Directive (eu) 2023/958 of the european parliment and of the council of 10 may 2023 amending directive 2003/87/ec as regards aviation's contribution to the union's economy-wide emission reduction target and the appropriate implementation of a global market-based measure," *Official Journal of the European Union*, 2023.

[8] M. Mansoor and N. Ejaz, "Thermal fatigue failure of fuel spray bars of a jet engine afterburner," *Engineering Failure Analysis*, vol. 18, pp. 492–498, 2011.

[9] O. Balli, "Turbine wheel fracture analysis of jet fuel starter (jfs) engine used on f16 military aircraft," *Engineering Failure Analysis*, vol. 128, 10 2021.

[10] G. J. D. Calabuig, A. Wilson, S. Bi, M. Vasile, M. Sippel, and M. Tajmar, “Environmental life cycle assessment of reusable launch vehicle fleets: Large climate impact driven by rocket exhaust emissions,” *Acta Astronautica*, vol. 221, pp. 1–11, 8 2024.

[11] “Space launch now database,” https://spacelaunchnow.me/launch/, accessed: 19.05.2024.

[12] B. Nigar, S. Dönmez, D. Çöker, and S. Özerinç, “Understanding mechanical failure of graphite rocket nozzle throats under thermal stresses,” *Aerospace Science and Technology*, vol. 119, 12 2021.

[13] X. Wang, X. Xu, and Q. Yang, “Numerical analysis on thermal environment of reusable launch vehicle during supersonic retropropulsion,” *International Journal of Thermal Sciences*, vol. 198, 4 2024.

[14] D. Krajcinovic and J. J. Carey, “Fluid-solid interaction of reactor core components, a preliminary analysis,” *Nuclear Engineering and Design*, vol. 31, no. 1, pp. 87–94, 1974.

[15] T. B. Belytschko and J. M. Kennedy, “A fluid-structure finite element method for the analysis of reactor safety problems,” *Nuclear Engineering and Design*, vol. 38, no. 1, pp. 71–81, 1976.

[16] T. Belytschko, “Methods and programs for analysis of fluid-structure systems,” *Nuclear Engineering and Design*, vol. 42, no. 1, pp. 41–52, 1977.

[17] K. Mori, “Response of the Bottom Plate of High Speed Crafts under Impulsive Water Pressure,” *Journal of the Society of Naval Architects of Japan*, vol. 1977, no. 142, pp. 297–305, 1977.

[18] D. D. Truong, B. S. Jang, C. E. Janson, J. W. Ringsberg, Y. Yamada, K. Takamoto, Y. Kawamura, and H. B. Ju, “Benchmark study on slamming response of flat-stiffened plates considering fluid-structure interaction,” *Marine Structures*, vol. 79, no. June, p. 103040, 2021.

[19] S. Turek and J. Hron, “Proposal for Numerical Benchmarking of Fluid-Structure Interaction between an Elastic Object and Laminar Incompressible Flow,” in *Fluid-Structure Interaction*, vol. 53, pp. 371–385, Berlin, Heidelberg: Springer Berlin Heidelberg, 2006.

[20] C. Stefanini, F. Giorgetti, A. Mercuri, A. Facci, and P. Fanelli, “Cylinder-lamina system fluid–structure interaction problem solved with an original OpenFOAM code,” *Journal of Computational Science*, vol. 54, p. 101420, sep 2021.

[21] P. J. Ziółkowski, T. Ochrymiuk, and V. A. Eremeyev, “Fluid–solid interaction on a thin platelet with high-velocity flow: vibration modelling and experiment,” *Continuum Mechanics and Thermodynamics*, oct 2022.

[22] S. Henclik, “Numerical modeling of water hammer with fluid–structure interaction in a pipeline with viscoelastic supports,” *Journal of Fluids and Structures*, vol. 76, pp. 469–487, jan 2018.

[23] H. Ullah, M. Hussain, N. Abbas, H. Ahmad, M. Amer, and M. Noman, “Numerical investigation of modal and fatigue performance of a horizontal axis tidal current turbine using fluid–structure interaction,” *Journal of Ocean Engineering and Science*, vol. 4, pp. 328–337, dec 2019.

[24] Y. Dai, Y. Wu, C. Yang, G. Huang, and C. Huang, “Numerical study on gust energy harvesting with an efficient modal based fluid-structure interaction method,” *Aerospace Science and Technology*, vol. 116, p. 106819, sep 2021.

[25] Z. Xie, J. Jiao, and S. Wrona, “The fluid-structure interaction lubrication performances of a novel bearing: Experimental and numerical study,” *Tribology International*, vol. 179, p. 108151, jan 2023.

[26] K. Czechowicz, J. Badur, and K. Narkiewicz, “Two-way FSI modelling of blood flow through CCA accounting on-line medical diagnostics in hypertension,” *Journal of Physics: Conference Series*, vol. 530, p. 012011, aug 2014.

[27] J. Badur and M. Bryk, “Accelerated start-up of the steam turbine by means of controlled cooling steam injection,” *Energy*, vol. 173, pp. 1242–1255, apr 2019.

[28] N. Hassanjanikhoshkroud, *A Thermal-Fluid-Structure Interaction Formulation Based on the Fictitious Domain Method: Simulation Studies with Applications to Geophysical Phenomena.* master thesis, Friedrich-Alexander-Universität Erlangen-Nürnberg, 2020.

[29] N. Hassanjanikhoshkroud, M. G. C. Nestola, P. Zulian, C. Von Planta, D. Vogler, H. Köstler, and R. Krause, “Thermo-Fluid-Structure Interaction Based on the Fictitious Domain Method: Application to Dry Rock Simulations,” *Proceedings*, pp. 1–12, 2020.

[30] J. Badur, P. Ziółkowski, W. Zakrzewski, D. Sławiński, S. Kornet, T. Kowalczyk, J. Hernet, R. Piotrowski, J. Felincjancik, and P. J. Ziółkowski, “An advanced Thermal-FSI approach to flow heating/cooling,” *Journal of Physics: Conference Series*, vol. 530, no. 1, 2014.

[31] P. Pironkov, *Numerical Simulation of Thermal fluid–Structure Interaction.* Phd thesis, Technischen Universitat Darmstadt, 2010.

[32] T. Gleim, P. Birken, M. Weiland, D. Kuhl, A. Meister, and O. Wünsch, “Thermal fluid-structure-interaction - Experimental and numerical analysis,” *AIP Conference Proceedings*, vol. 1648, no. March, pp. 1–6, 2015.

[33] S. Willems, B. Esser, and A. Gülhan, “Experimental and numerical investigation on thermal fluid–structure interaction on ceramic plates in high enthalpy flow,” *CEAS Space Journal*, vol. 7, no. 4, pp. 483–497, 2015.

[34] W. Huang, C. Liao, X. Liu, S. Suo, Y. Liu, and Y. Wang, “Thermal fluid-solid interaction model and experimental validation for hydrostatic mechanical face seals,” *Chinese Journal of Mechanical Engineering (English Edition)*, vol. 27, no. 5, pp. 949–957, 2014.

[35] S. Dhar and A. Vacca, “A novel FSI-thermal coupled TEHD model and experimental validation through indirect film thickness measurements for the lubricating interface in external gear machines,” *Tribology International*, vol. 82, no. PA, pp. 162–175, 2015.

[36] B. Kraszewski, “A study of thermal effort during half-hour start-up and shutdown of a 400 MW steam power plant spherical Y-pipe,” *Case Studies in Thermal Engineering*, vol. 21, no. June, p. 100728, 2020.

[37] W. Burzyński, “Theoretical foundations of the hypotheses of material effort,” *Czasopismo Techniczne*, vol. 47, pp. 1–41, 1929.

[38] K. Banaś and J. Badur, “Influence of strength differential effect on material effort of a turbine guide vane based on thermoelastoplastic analysis,” *Journal of Thermal Stresses*, vol. 40, no. 11, pp. 1368–1385, 2017.

[39] W. Dudda and B. Kraszewski, “A theoretical validation of Burzyński hypothesis for a stress-strain analysis of heat-resistant steel,” *Case Studies in Thermal Engineering*, vol. 23, 2021.

[40] N. A. Nariman, “Thermal fluid-structure interaction and coupled thermal-stress analysis in a cable stayed bridge exposed to fire,” *Frontiers of Structural and Civil Engineering*, vol. 12, no. 4, pp. 609–628, 2018.

[41] A. Franci, E. Oñate, J. M. Carbonell, and M. Chiumenti, “PFEM formulation for thermo-coupled FSI analysis. Application to nuclear core melt accident,” *Computer Methods in Applied Mechanics and Engineering*, vol. 325, pp. 711–732, 2017.

[42] H. S. Joo, H. Cho, Y. Lee, S. J. Shin, J. J. Yoh, and J. C. Shin, "Parametric study of a VLS based on 2-D FSI analysis," *Aerospace Science and Technology*, vol. 84, pp. 530–542, 2019.

[43] T. Ochrymiuk, M. Banaszkiewicz, M. Lemanski, T. Kowalczyk, P. Ziółkowski, P. J. Ziółkowski, R. Hyrzynski, M. Stajnke, M. Bryk, B. Kraszewski, S. Kruk-Gotzman, M. Froissart, and J. Badur, "Fluid solid interactions - a novelty in industrial applications," *Archives of Thermodynamics*, vol. 43, no. 2, pp. 75–96, 2022.

[44] C. Hirsch, *Numerical Computation of Internal and External Flows.* Elsevier, 2 ed., 2007.

[45] Y. Fung, *Foundations of solid mechanics.* Englewood Cliffs: Prentice-Hall, Inc., 1965.

[46] W. Nowacki and Z. S. Olesiak, *Termodyfuzja w ciałach stałych.* Warszawa: PWN, 1991.

[47] C. Hirt and B. Nichols, "Volume of fluid (VOF) method for the dynamics of free boundaries," *Journal of Computational Physics*, vol. 39, pp. 201–225, jan 1981.

[48] ANSYS, "Ansys Fluent Theory Guide," 2019.

[49] D. L. Youngs, *Time-dependent multi-material flow with large fluid distortion.* Academic Press Inc. (London) Ltd., 1982.

[50] J. U. Brackbill, D. B. Kothe, and C. Zemach, "A continuum method for modeling surface tension," *Journal of Computational Physics*, vol. 100, no. 2, pp. 335–354, 1992.